BOMEM

NGST

Next Generation Space Telescope

Final Report

Volume 4 - Performance Analyses

Document Number: **SP-BOM-008/99**

Issue: **1** **Revision:** A

Issue Date: **13 October 1999** **Document Name:** Annex B4.doc

	Function	Name	Signature	Date
Prepared by	Scientist	Louis Moreau		
Prepared by	Scientist	Pierre Tremblay		
Approved by	Project Manager	André Villemaire		
Approved by	Director, SPR division	Jean Giroux		

BOMEM Inc. • a unit of Elsag Bailey Process Automation N.V.

450 Saint-Jean-Baptiste Avenue • Québec, Québec G2E 5S5 Canada • Phone (418) 877–2944 • Fax (418) 877–2834

TABLE OF CONTENTS

LIST OF FIGURES

LIST OF TABLES

DOCUMENT CHANGE RECORD

Issue	Rev.	Date	Chapter/Paragraph Number, Change Description (and Reasons)
1(draft)	-	15 February 1999	Draft of document
1	-	16 March 1999	First release of document
1	A	13 October 1999	New revision to remove proprietary notices.

1. INTRODUCTION

1.1 BACKGROUND INFORMATION

The Next Generation of Space Telescope (NGST) project of NASA is intended to provide continuity and new focus for research following the success of the Hubble Space Telescope. It is considered to be a technologically challenging project as the technology needed is not necessarily available. It challenges the innovation of the scientific and technological community to come up with an affordable technology to carry out the scientific goals of the mission.

Canada has a strong Space Astronomy community and they have ranked the participation of this project as the priority in their LTSP III submission. In order for Canada to participate, the areas of technical expertise and competence necessarily has to match the required technologies of the NGST project. The nature and scope of the Canadian contribution to the NGST are neither identified nor defined. The CSA sees the Canadian contribution as one that matches the industrial capability, an area that would result in industrial and economic growth and provide a sound base for competitiveness in the international market.

At the end of 1998, CSA awarded a number of contracts to Canadian firms. Bomem was awarded such a contract to study the potential use of a Fourier Transform Imaging Spectrometer as a science instrument for NGST.

1.2 SCOPE OF PROJECT

This work was carried out under contract no 9F007-8-3007/001/SR.

Bomem proposed to study the potential use of a Imaging Fourier Transform Spectrometer as a moderate spectral resolution camera for NGST. The approach was to first investigate the trade space of the instrument design. Next the performance of the instrument was predicted to confirm the suitability of the technology for the NGST mission. The risk analysis and mitigation plans were then completed. Finally the Cost and Schedule estimates were drafted based on the previous findings.

1.3 SCOPE OF DOCUMENT

This document is Volume 4 of the final report. The other deliverables of the study contract are listed in Table 1.

Volume 4 covers the *Performance Analyses* performed on the contribution proposed by Bomem, namely an Imaging Fourier Transform Spectrometer (IFTS) module as one of the central science instrument for NGST. The goal of a performance analyses is to evaluate the performance of the proposed IFTS against the science objectives of NGST. The document examines several performance-related issues. In Section 2 we estimate the basic sensitivity of the NGST IFTS. Photon noise and sampling position noise is studied. The sampling position noise is a type of noise not usually encountered in standard Fourier Transform Spectrometer (FTS) and is due to the very slow operation of the NGST IFTS. Section 3 covers the spectral characteristics such as spectral resolution and lineshape characteristics. In Section 4, the sensitivity of Fourier Transform Spectrometers is compared to competing spectrometer technologies such as dispersive systems and filter systems. This is of great

interest in the debate aiming to elect the best spectrometer for NGST. Finally Section 5 addresses some FTS-specific modes of operation, in order to optimise the IFTS sensitivity.

Table 1: Deliverables of the study contract

Volume	Document Number	Document	Description
1	SP-BOM-005/99	Executive Summary	5-page summary of the findings of the contract
2	SP-BOM-006/99	Planning Report	Report on the scheduling and cost of the proposed Canadian participation. The planning report also includes the risk assessment and mitigation plan
3	SP-BOM-007/99	Trade Analyses	Report on the trade analyses performed to arrive at a credible baseline for the proposed Canadian participation.
4	SP-BOM-008/99	Performance Analyses	Report on the sensitivity analyses performed to evaluate the suitability of the proposed Canadian participation for NGST
5	SP-BOM-009/99	Technology Report	Report on some proposed novel technology approaches to the specific NGST environment for the proposed Canadian participation.

1.4 REFERENCE DOCUMENTS

RD 1 Bomem Proposal No:SPIR180898, issue 1, revision -, dated 8 September 1998, in response to solicitation No 9F007-8-3007/A.

RD 2 Volume 4 - Performance Analyses NGST performance studies, SP-BOM-008/99

OPP89 A. V. Oppenheim and R. W. Schafer, “Discrete-time signal processing”, Prentice-Hall International, London, 1989, p. 530.

PAP91 A. Papoulis, “Probability, Random Variables and Stochastic Processes”, 3rd edition, McGraw-Hill, New York, 1991.

PRI97 A. T. Pritt, Jr., P. N. Kupferman, S. J. Young, R. A. Keller, “Imaging LWIR spectrometers for remote sensing applications”, SPIE Proceedings 3063, 1997.

1.5 DEFINITIONS

Étendue — The product of the limiting collection area and the solid angle of the limiting field of view. Often called throughput.

Irradiance — Incident radiant energy per unit surface per unit time. Spectral Irradiance is the irradiance at a given wavenumber (or wavelength or frequency) per unit wavenumber (or unit wavelength or unit frequency). Usual symbol is *E*.

Jansky — Units of spectral irradiance. Symbol is Jy (1 Jy = 10^{-26} W m^{-2} s).

Radiance — Radiant energy per unit surface per unit solid angle per unit time. Spectral radiance is the radiance at a given wavenumber (or wavelength or frequency)

per unit wavenumber (or unit wavelength or unit frequency). Usual symbol is *L*.

Wavenumber — The inverse of the wavelength. Usual symbol is σ (σ=1 /λ).

1.6 ACRONYMS

AC	Alternating Current
CCD	Charge-Coupled Device
CSA	Canadian Space Agency
DC	Direct Current
DF	Dispersive Filter
DFT	Discrete Fourier Transform
DN	Detector Noise
DSI	Double-Sided Interferogram
FFT	Fast-Fourier Transform
FOV	Field Of View
FOV	Field Of View
FPA	Focal Plane Array
FPA	Focal Plane Array
FSR	Free Spectral Range
FTS	Fourier Transform Spectrometer
FTS	Fourier-Transform Spectrometer
FWHM	Full-Width at Half Maximum
IFIRS	Integral Field Infrared Spectrograph
IFS	Integral Field Spectrograph
IFTS	Imaging Fourier Transform Spectrometer
IR	Infrared
MIR	Middle Infrared
MOS	Multi-Object Spectrograph
MPD	Maximum path difference
NEP	Noise Equivalent Power
NESI	Noise Equivalent Spectral Irradiance
NESR	Noise Equivalent Spectral Radiance
NGST	New Generation Space Telescope
NGST	Next Generation Space Telescope
NIR	Near Infrared
OPD	Optical path difference
PN	Photon Noise
RMS	Root-Mean Squared

RN	Read-Out Noise
SNR	Signal to Noise Ratio
SNR	Signal to Noise Ratio
SSI	Single-Sided Interferogram
TF	Tuneable Filter
VIS	Visible
ZPD	Zero Path Difference

2. IFTS SENSITIVITY

It this section, we perform a sensitivity calculation for the NGST IFTS. The goal is to confirm that the IFTS can indeed meet the scientist requirements.

In our simulations we model two sources of noise: the photon noise and the noise due to errors of position of the moving mirror in the interferometer are evaluated. Other sources of noise such as the detector dark current, the digitisation noise, etc., are not considered because it is expected that the technology used will be such as to make these sources of noise negligible compared to the photon noise.

2.1 PHOTON NOISE

The noise equivalent spectral power due to photon noise is:

$$NEP_\gamma(\sigma) = \frac{I_N \, h \sigma \, c}{\eta(\sigma) \, q} \tag{1}$$

where

h: Planck's constant (6.63×10^{-34} J s)

c: speed of light (3.00×10^{8} m s^{-1})

q: elementary charge (6.19×10^{-19} C)

η: spectral quantum efficiency of the detector

σ: wavenumber (m^{-1})

I_N: Current noise (A $s^{0.5}$)

The current noise is proportional to the square root of the total detector current. For a photovoltaic detector, the current noise is:

$$I_N = \sqrt{2 \, q \, I} \tag{2}$$

where, I is the total detector current (per pixel):

$$I = \int_0^\infty q \, \eta(\sigma) \, \Phi_\gamma(\sigma) \, d\sigma \tag{3}$$

where $\Phi_\gamma(\sigma)$ is the total spectral photon flux reaching a pixel of the detector:

$$\Phi_\gamma(\sigma) = \frac{\Phi(\sigma) + \Phi_z(\sigma) + \Phi_d(\sigma)}{h \, c \, \sigma} \tag{4}$$

where $\Phi(\sigma)$ is the spectral energy flux from the target reaching a pixel of the detector. $\Phi_z(\sigma)$ is the spectral zodiacal energy flux reaching a pixel of the detector. $\Phi_d(\sigma)$ is the spectral energy flux emitted by the instrument reaching a pixel of the detector.

$$\Phi(\sigma) = \xi(\sigma)\Theta L(\sigma) \tag{5}$$

$$\Phi_z(\sigma) = \xi(\sigma)\Theta L_z(\sigma) \tag{6}$$

$$\Phi_d(\sigma) = \Theta L_d(\sigma) \tag{7}$$

where $\xi(\sigma)$ is the interferometer efficiency, Θ is the instrument étendue, $L(\sigma)$ is the spectral radiance of the target, $L_z(\sigma)$ is spectral zodiacal radiance (radiation reflected and emitted by interplanetary dust) and $L_d(\sigma)$ is the radiance emitted by the instrument itself. The interferometer efficiency is:

$$\xi(\sigma) = \frac{\xi_{DC}(\sigma)\xi_{AC}(\sigma)}{2} \tag{8}$$

where $\xi_{DC}(\sigma)$ is the spectral transmission efficiency and $\xi_{AC}(\sigma)$ the spectral modulation efficiency. For this instrument, the étendue is the product of the area of the entrance pupil (taken to be equal to the area of the primary telescope) times the solid angle of the field of view of one pixel:

$$\Theta = \pi R^2\ \Omega = \pi\, r^2\ \theta^2 \tag{9}$$

r is the radius of the telescope is and θ is the edge field of view angle for a pixel, assumed to be square.

For this study the spectral radiance of the target, $L(\sigma)$, is the radiance of a blackbody of temperature T with a red shift of z multiplied by a "fill factor" f to reduce the radiance to appropriate level:

$$L(\sigma) = f\ \frac{2hc^2\left[\sigma(z+1)\right]^3}{e^{\frac{hc\sigma(z+1)}{kT}} - 1} \tag{10}$$

where k is Boltzman constant (1.38×10^{-23} J K^{-1}).

The radiance of the zodiacal light is:

$$L_z(\sigma) = \tau_s \frac{2hc^2\sigma^3}{e^{\frac{hc\sigma}{kT_\odot}} - 1} + \tau_{th} \frac{2hc^2\sigma^3}{e^{\frac{hc\sigma}{kT_{th}}} - 1} \tag{11}$$

with:

$$\tau_{th} = 5.61\times10^{-8}\, d^{-0.8} \ \text{(unitless)} \tag{12}$$

$$T_{th} = 266\, d^{-0.36} \quad (\text{in K}) \tag{13}$$

$$\tau_s = \frac{\tau_{th}\,\alpha}{1-\alpha}\left(\frac{T_{th}}{T_\odot}\right)^4 \tag{14}$$

where d is the distance between NGST and the sun in astronomical units, α is the albedo of the dust particles and $T_\odot$ is the Sun temperature in Kelvin.

The radiance emitted by the instrument is the radiance emitted by a black body at the instrument's temperature with an emissivity equal to its overall absorptance:

$$L_d(\sigma) = (1-\xi_{DC})\frac{2hc^2\sigma^3}{e^{\frac{hc\sigma}{kT_d}}-1} \tag{15}$$

where T_d is the temperature of the instrument.

To covert the spectral NEP into NESR, the étendue of the instrument, Θ, its efficiency, $\varepsilon(\sigma)$, the integration time, t, and the spectral interval, $\Delta\sigma$, must be considered:

$$NESR_\gamma(\sigma) = \frac{NEP_\gamma(\sigma)}{\sqrt{n}\,\Delta\sigma\,\Theta\,\xi(\sigma)\,F\,\sqrt{t}} \tag{16}$$

where F is the apodization factor. F=1 for unapodized spectra. n is equal to 1 for a single-port instruments, and to 2 for a dual port instruments. The spectral resolution is the difference between the maximum and the minimum wavenumber for the band studied divided by the "resolution factor", R:

$$\Delta\sigma = \frac{1}{2MPD} = \frac{\sigma_{\max}-\sigma_{\min}}{R} \tag{17}$$

R corresponds to number of bands sampled. It is an integer number between $\sigma_{\max}$–$\sigma_{\min}$ (corresponding to the finest spectral interval considered, 1 cm^{-1}) and 1 (corresponding to a single broad spectral band). MPD is the maximum optical path difference between the two arms of the interferometer.

2.2 POSITION ERROR

The mirror in the moving arm of the interferometer can be positioned with a finite precision. Position errors cause errors in the sampling of the interferogram and these sampling errors cause artifacts and noise in the acquired spectra. Evaluating this noise will give an idea of the required position accuracy.

The noise due to the position errors cannot easily be evaluated analytically. We have to use a Monte-Carlo simulation. The computation can be described by the following steps:

1) Compute the theoretical total spectral radiance incoming on the detector:

$$L_T(\sigma) = \xi(\sigma)L(\sigma) + \xi(\sigma)L_z(\sigma) + L_d(\sigma) \tag{18}$$

2) Compute the theoretical interferogram as being the real part of the Fourier transform of the incoming radiance:

$$I(x) = \Re\{F\{L_T(\sigma)\}\} \tag{19}$$

3) The theoretical interferogram is interpolated by a Fourier transform process to increase its resolution by a factor 8.

4) A new perturbed interferogram is created by sampling the interpolated interferogram at the selected resolution plus a random position error. The sampling positions are:

$$x = N\,\Delta x + \delta x(s_x)\,\Delta x \tag{20}$$

where N is the sampling position number, Δx is the sampling interval and $\delta x(s_x)$ is a random number from a Gaussian distribution of standard deviation s_x. s_x is the relative position error. A new random number is generated for every sampling position.

5) The perturbed interferogram is Fourier transform to generate a perturbed spectrum.

6) Steps 4 and 5 are repeated a sufficient number of time to generate a good statistics. For this study, the process was repeated 50 times.

7) The standard deviation of all the perturbed spectra generated is computed at every wavenumber. The NESR due to the position error, $NESR_\delta$, is that spectral standard deviation.

2.3 TOTAL NOISE

Neglecting the other sources of noise, the total NESR is simply the root sum squared of the NESR due to the photon noise and the NESR due to the position error:

$$NESR(\sigma) = \sqrt{NESR_\gamma^2(\sigma) + NESR_\delta^2(\sigma)} \tag{21}$$

The signal to noise ratio (SNR) is the radiance of the target divided by the total NESR:

$$SNR(\sigma) = \frac{L(\sigma)}{NESR(\sigma)} \tag{22}$$

2.4 RESULTS

Some results are presented to establish a base performance and to illustrate the effect of the various parameters of interest. The following parameters define the base case and have been keep constant for all tests, unless otherwise mentioned:

Radius of primary telescope:	r = 4 m
FOV of one pixel:	θ = 0.05"
Acquisition time:	$t = 2\times10^6$ s
Resolution factor:	R = 100
Transmission efficiency:	ξ_{DC} = 0.84
Modulation efficiency:	ξ_{AC} = 0.70
N. of output port::	n = 1
Apodization factor:	F = 1
Temperature of instrument:	T_d = 30 K

Minimum wavenumber: σ_{min} = 2000 cm^{-1} (corresponding to 5 μm)

Maximum wavenumber: σ_{min} = 10000 cm^{-1} (corresponding to 1 μm)

Quantum efficiency: η = 0.95 from σ_{min} to σ_{max} , 0 elsewhere

Orbital distance: d = 1 A.U.

Albedo of interplanetary dust: α = 0.102

Sun temperature: $T_{\odot}$ = 5770 K

Temperature of the target: T = 5800 K

Red shift of the target: z = 5

Fill factor: $f = 3.7\times10^{-14}$

Relative sampling position error (rms): s_x = 1%

2.4.1 Photon Noise Only

For this step the position error is set to zero. The only noise present is the photon noise.

The target is a blackbody with a temperature T of 5800 K and a red shift z of 5. The "fill factor" f is set to 3.7×10^{-14} on order to have an irradiance of about 5 nJ at a wavelength of 3 μm. Figure 1 shows the spectral irradiance of the target in nJy. Figure 2 shows the spectral photon flux at the detector. Compared to the zodiacal light, the flux emitted by the instrument is negligible for an internal temperature of 30K. The background photon noise is dominated by the zodiacal light.

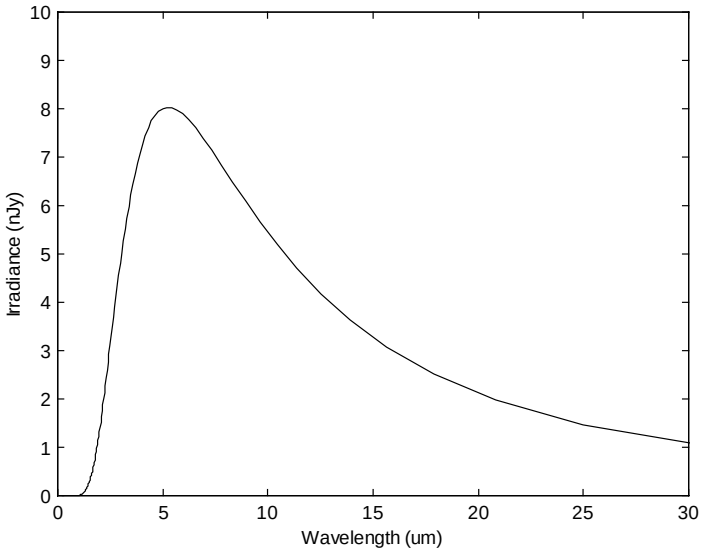

Figure 1 Target spectral irradiance

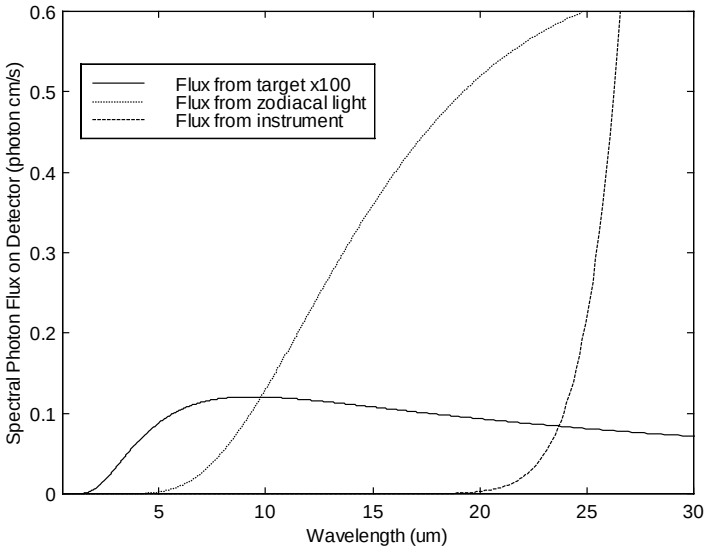

Figure 2 Spectral photon flux on detector

For the first case, the SNR has been computed in the band extending from 1 μm to 5 μm for a resolution factor, *R*, of 100. Figure 3 shows the NESR and the NESI for that case study. Figure 4 shows the SNR as a function of the wavelength. When there is no other noise than the photon noise, Equations 16, 17 and 22 show that the SNR is directly proportional to R^{-1} and directly proportional to $t^{-½}$. There is no need to recalculate different cases to determine the effect of *R* and *t*. For instance at full spectral resolution (R=8000) and every other parameters being constant, the SNR will be 80 time smaller than the SNR plotted on Figure 4. At the broadest spectral resolution (*R*=1), the SNR will be higher by a factor 100 than the SNR of Figure 4.

Similarly, if the flux from emitted by the instrument is negligible, the SNR will be directly proportional to $\sqrt{\xi}$ and to $\sqrt{\Theta}$. Increasing the spectrometer efficiency or the étendue of the instrument increases the SNR. For the current case study, the efficiency is $\xi = 0.3$. Increasing the efficiency to a perfect value ($\xi = 0.5$) will increase the SNR by factor 1.3 compared to the SNR of Figure 4.

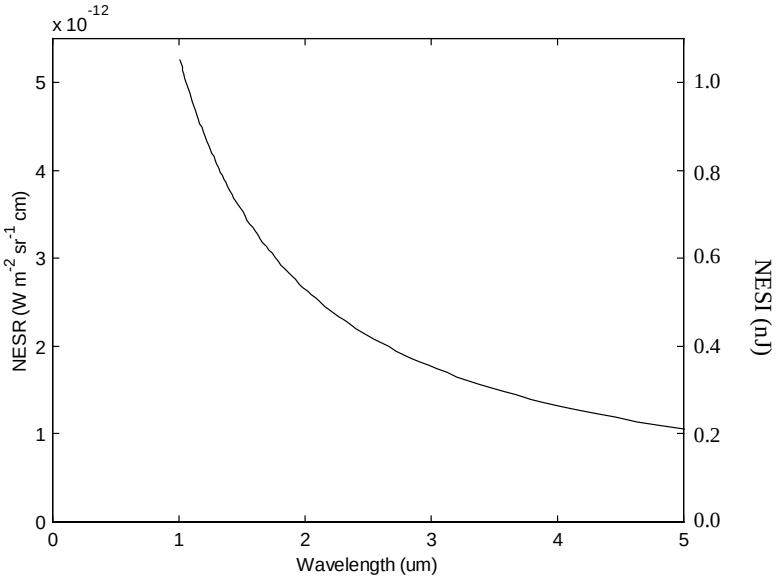

Figure 3 Noise Equivalent Spectral Radiance (NESR) and noise equivalent Spectral Irradiance (NESI) for case 1

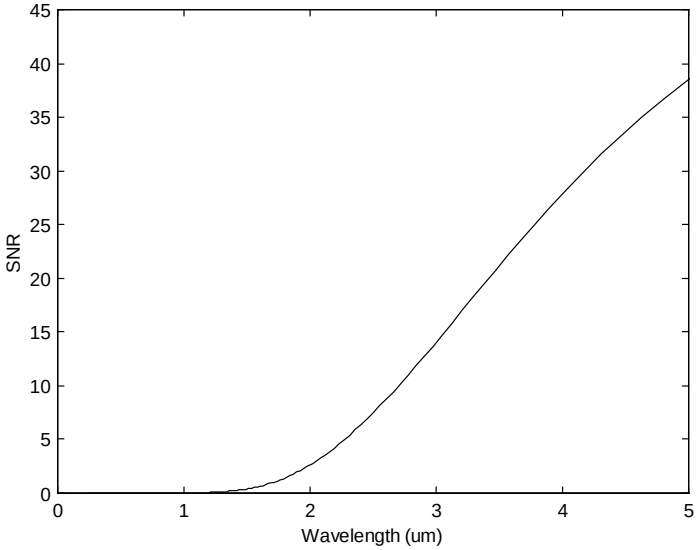

Figure 4 Signal to noise ratio for case 1

The SNR also depends on the incoming radiance, L (i.e. the signal). Because the photon noise is proportional to the square root of the photon flux incoming on the detector, the SNR would be proportional to $\sqrt{L}$ if the background radiation was negligible. In our case, the zodiacal light is important compared to the signal and the dependency of the SNR on L is slightly more complex. Figure 5 compares the SNR of the base case (i.e. Figure 4) compared to the signal for 2*f* and for 0.5*f*.

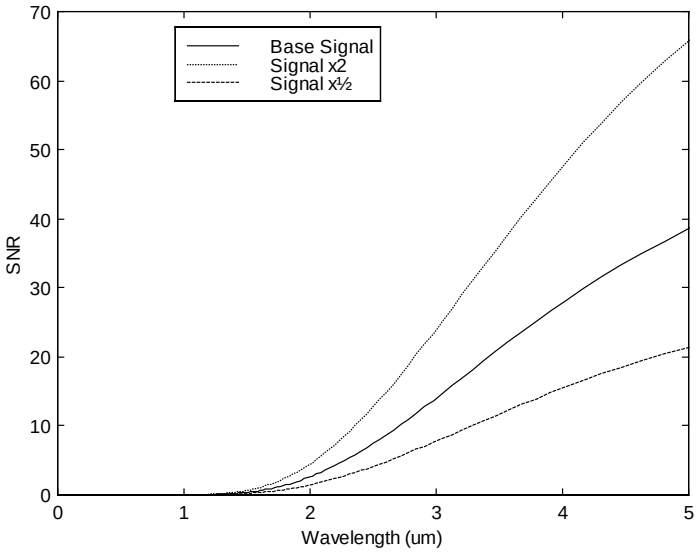

Figure 5 SNR for various signal level

2.4.2 Position Error Noise Only

In this section we describe the effect of errors the position of the sampled interferogram points. Interferograms sampled at the wrong positions appear to have amplitude error which translate into system noise. The process of simulating the sampling position errors is illustrated in Figure 6. The same input parameters listed in Section 2.4.1 were used to compute the total signal.

Figure 7 shows 3 curves of NESR caused by sampling position errors only (i.e. no photon noise) for three different relative rms position errors. $NESR_\delta$ is directly proportional to s_x. Since the signal is not affected by sampling errors, the SNR is thus directly proportional to s_x^{-1}. Because, the noise is computed for relative errors, the calculations are independent of the selected spectral interval. If the absolute error is constant, the SNR will be proportional to R^{-1}.

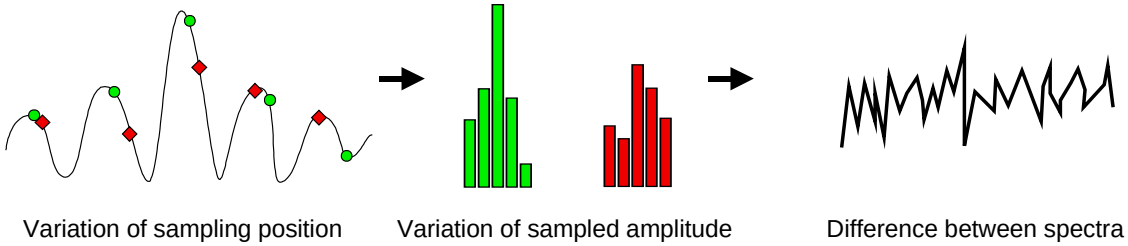

Figure 6 Illustration of the sampling position errors

The fine spectral shape of the NESR curves of Figure 7 depends in part on the random nature of the Monte-Carlo simulations and in part on the shape of the interferogram and, thus, on the spectral

shape of the incoming radiance. However, overall, the shape is spectrally flat and the noise caused by the sampling position error can be considered to be white.

The noise caused by the sampling position error is proportional to the amplitude of the interferogram, so it is proportional to the amplitude of the total incoming radiance. Because the background light is not negligible for small incoming flux, $NESR_\delta$ is only approximately proportional to the signal level. To illustrate this, Figure 8 shows three curves of $NESR_\delta$ for three different signal level. So, if the position error noise is dominant, the SNR is independent of the total signal level.

The noise caused by the sampling position error is proportional to the amplitude of the interferogram. The amplitude of the interferogram is proportional to the total energy reaching the detector, so it is proportional to the system efficiency, ξ, and étendue, Θ. So the noise in term of photon flux is proportional to ξ and Θ. However the gain is inversely proportional to ξ and Θ so that the calibrated noise ($NESR_\delta$) is independent of the efficiency and étendue.

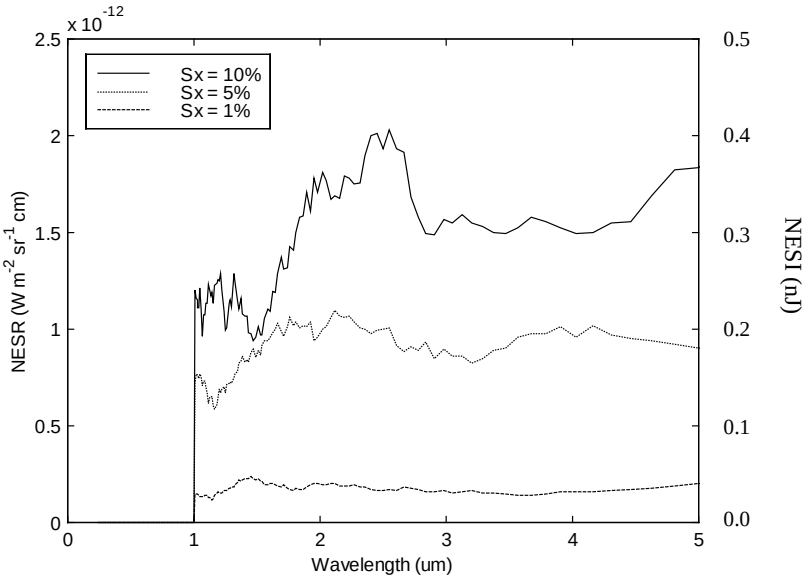

Figure 7 NESR due to the position error for various relative errors of sampling position

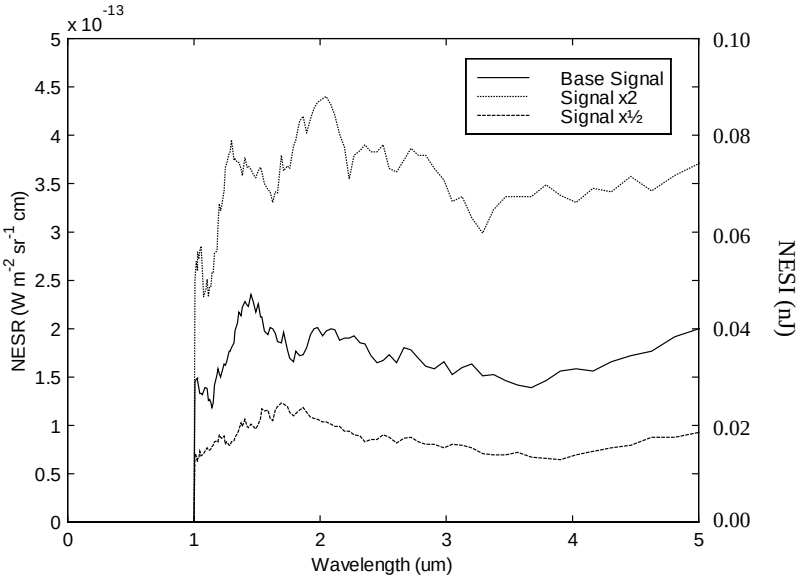

Figure 8 NESR due to the position error for various signal levels and a position error of 1% (rms)

2.4.3 Summary

For the photon noise, analysis of the equations of Section 2.1 and the results shown in Section 2.4.1, lead to the following conclusions:

$$NESR_\gamma \propto \sqrt{\int L\, d\sigma}$$
$$NESR_\gamma \propto R$$
$$NESR_\gamma \propto \frac{1}{\sqrt{t}}$$
$$NESR_\gamma \propto \frac{1}{\sqrt{\xi}}$$
$$NESR_\gamma \propto \frac{1}{\sqrt{\Theta}}$$
$$NESR_\gamma \propto \sigma$$

For the position error noise, analysis of the equations of sections 2.1 and 2.2 and the results shown in Section 2.4.2, lead to the following conclusions:

$$NESR_\delta \propto L$$
$$NESR_\delta \propto s_x$$
$$NESR_\delta \propto R$$
$$NESR_\delta \text{ is spectrally flat}$$
$$NESR_\delta \text{ is independent of } t,\ \xi \text{ and } \Theta$$

Comparison of Figure 3 and Figure 7 indicates that for an irradiance of about 5nJy at a wavelength of 3 μm and a sampling position accuracy of 1%, the photon noise is more than 10 times larger than the position error noise. A position accuracy of 1% is readily achievable with a modern servo-control, so it should not be difficult to achieve a SNR of more than 10 for signals of about 5 nJy with the current design. Having a high efficiency and a high étendue would also rise the SNR for small incoming fluxes.

Because $NESR_\delta$ is proportional to the signal and $NESR_\gamma$ is proportional to the square root of the signal, $NESR_\delta$ increases more rapidly with the signal than $NESR_\gamma$. So, even if $NESR_\gamma$ is much larger than $NESR_\delta$ for small signals, at some point, for larger signals, $NESR_\delta$ will be higher than $NESR_\gamma$. Of course, at this point the SNR may large enough to satisfy most practical applications. Figure 9 shows both $NESR_\delta$ and $NESR_\gamma$ as a function of the signal level. $NESR_\gamma$ exceeds $NESR_\delta$ when the signal is about fifty times the base case signal. Figure 10 shows the corresponding SNR. For figures 8 and 9, all parameters, except *f*, are as stated for the base case of Section 2.4.

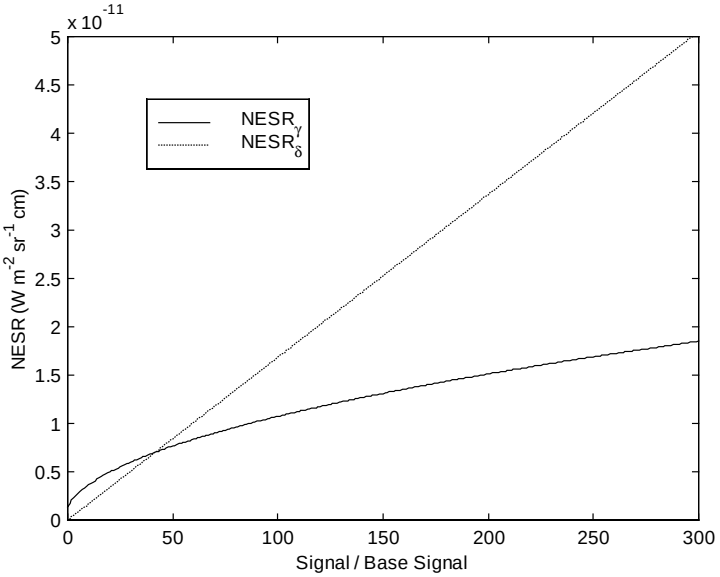

Figure 9 $NESR_\gamma$ and $NESR_\delta$ as a function of the signal level at a wavelength of 3 μm

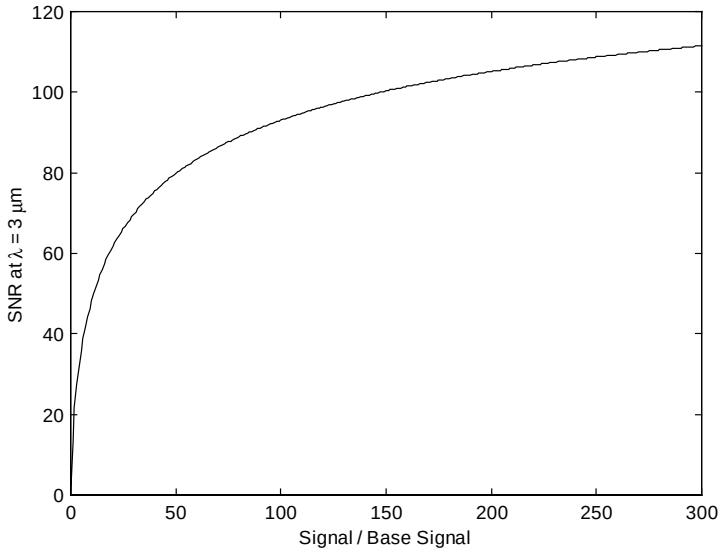

Figure 10 Signal to noise ratio at a wavelength of 3 µm as a function of the signal level

3. IFTS INSTRUMENT LINESHAPE

In this section we describe the instrument lineshape (ILS) simulations made the NGST IFTS. The goal of these activities is both to design the interferometer and to predict the performance.

As a design tool the ILS models are used to determine the maximum angle permissible in the interferometer. For a constant throughput (as set by the NGST telescope), the larger the angles in the interferometer, the smaller the interferometer pupil can be. However there exists a limit beyond which the instrument lineshape degrades and consequently the spectral resolution decreases below the science requirements.

One such example is shown in Figure 11, where the full width at half maximum of the lineshape is plotted against the full angle in the interferometer. If we take the 64x64 example, we can see the lineshape start to degrade for angles larger than 100 mrad. Other cases of larger detectors (256x256 and 1024x1024) show that the same degradation occurs at larger angles, because for the same total angle, there is a smaller angle on each individual pixel.

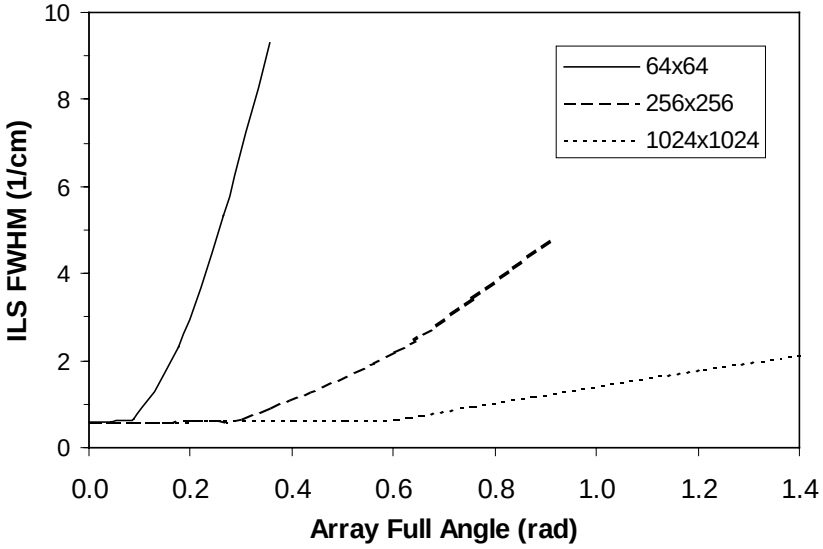

Figure 11 Full-width at half maximum of the instrumental line shape for the corner pixel at 2800 cm^{-1} against the array full angle for a MPD of 1 cm and various detector formats

We used our proprietary ILS model to simulate the lineshape characteristics of the NGST IFTS. We assumed a flat-mirror four-port design. In this configuration the detector layout is as shown in Figure 12. 10% of the detector width is left in between the input and output fields to allow space for a dissector.

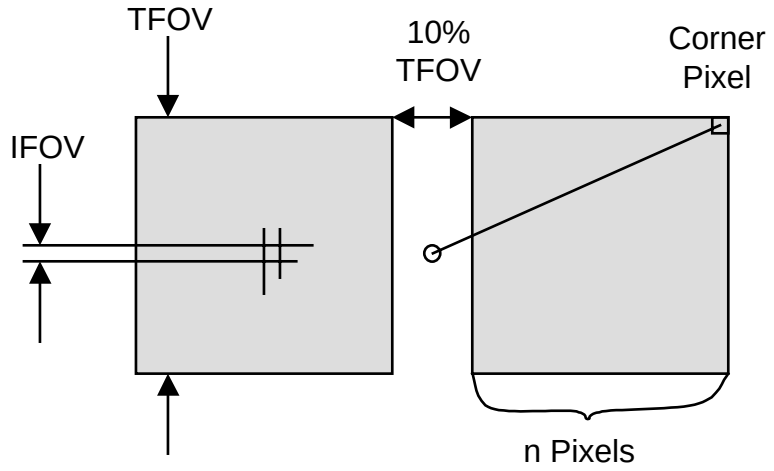

Figure 12 Focal configuration for a flat-mirror four-port interferometer. 10% of the detector width is left in between the input and output fields to allow space for a dissector.

All the simulations we done for the corner pixel which is always worse than any other pixel. The other simulation parameters are listed in Table 2. Several simulations were performed for both the highest wavenumber of both spectral bands, MIR and NIR. The NIR covers the 0.6-5.6 μm range while the MIR covers the 5.6-15 μm range. Various magnification ratio (angle in the interferometer over angle in the scene) were studied with the interferometer aperture varying accordingly.

Table 2: ILS parameters

	MIR	*NIR*
Wavenumber	1786 cm^{-1}	16 666 cm^{-1}
Detector Format	1 k x 1 k	8 k x 8 k
Total Scene Angle	1.7 arcmin	5.3 arcmin
Maximum Path Difference	1 cm	1 cm
Magnification	Various (5-160)	Various (5-160)
Interferometer Pupil	Various (160-5 cm)	Various (160-5 cm)

Figure 13 shows the variation of the linewidth as a function of interferometer aperture diameter. Negligible effects can be seen for aperture sizes as small as 4 cm. Figure 14 show an example of lineshape simulated. Consequently it appears that the angle effects will not be the limiting factor in choosing an interferometer configuration for the NGST IFTS. In fact the interferometer angles corresponding to the interferometer aperture diameter are shown in Figure 15. A reasonable interferometer pupil of 10 cm leads to about 8 degree angles. This is a reasonable choice and it is surprisingly similar to interferometer parameters used for existing of interferometer instruments in development today. This fact tends to reduce the risk.

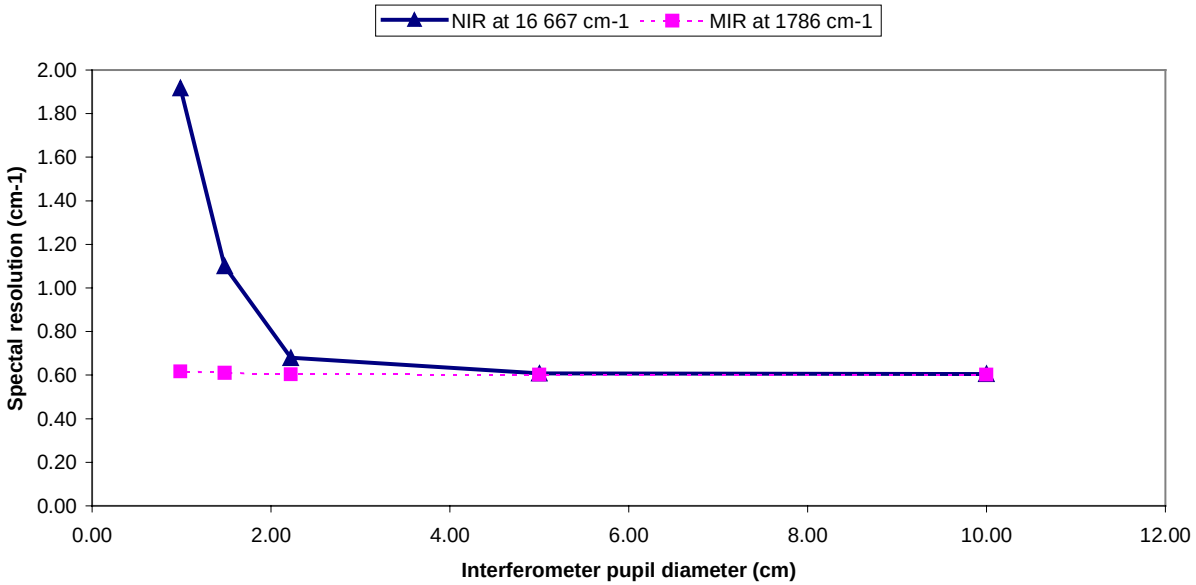

Figure 13 Full-width at half maximum of the instrumental line shape for both the MIR and NIR corner pixels as a function of interferometer aperture

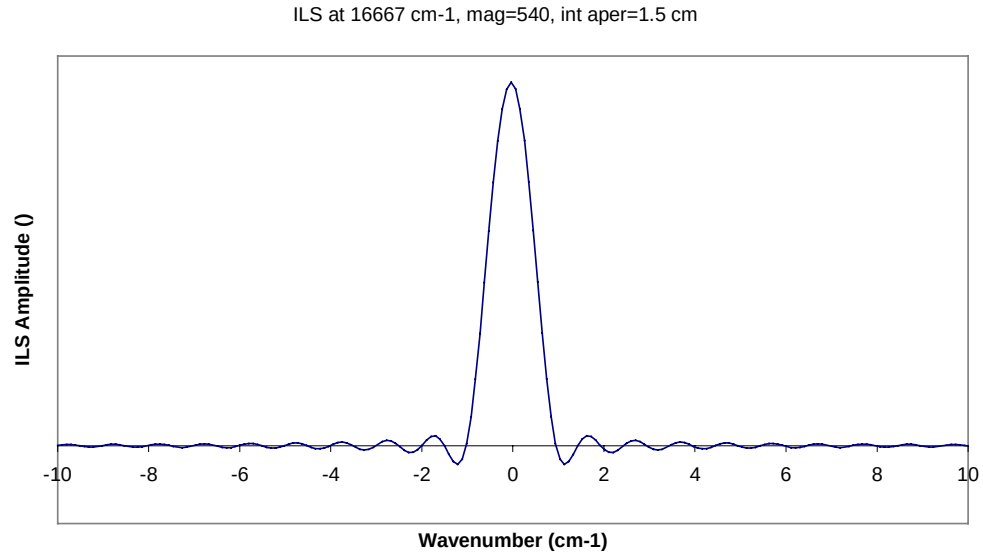

Figure 14 NIR lineshape example of an extreme NGST IFTS configuration, wit a 1.5 cm interferometer pupil.

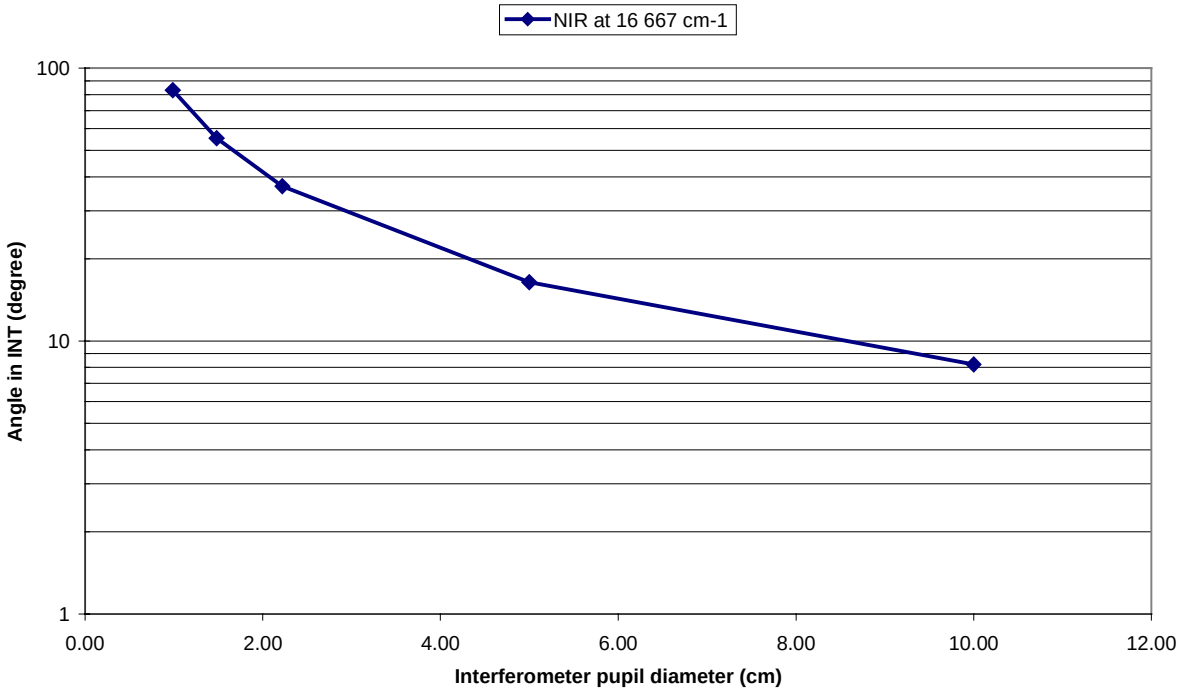

Figure 15 Full-width at half maximum of the instrumental line shape for both the MIR and NIR corner pixels as a function of interferometer aperture

4. IFTS SENSITIVITY COMPARISON

4.1 INTRODUCTION

This section provides a coherent evaluation of the sensitivity of various imaging spectrometers that can be used for NGST. The signal to noise ratio (SNR) is used as the basis of the comparison. The instruments evaluated in this study are spectrometers based on tuneable or dispersive filters, as well as Fourier-transform spectrometers. The performance of the imaging spectrometers is studied for integral field and multi-object spectrographic applications.

The single criterion of the SNR cannot be used alone to favour one option or another. Other aspects such as throughput and resolution must also be considered. Some requirements may moreover form a lock-up specification, forcing the choice to a particular instrument even if it is strongly disadvantaged when one aspect is studied. For example, in this study the spectrometers are compared for a constant throughput and resolution. But for any of these two parameters it can be technically hard or impossible to meet the needed specifications for a given instrument, thus reducing considerably the interest for this option. Pritt *et al.* (PRI97) gives an interesting overview of imaging spectrometers approaches, enumerating many aspects to be considered in order to compare them.

4.2 SENSITIVITY OF IMAGING SPECTROMETERS

In this section we evaluate the signal to noise ratio (SNR) performance of different imaging spectrometer configurations. We consider instruments using tuneable filters (TF), dispersive filters (DF) or Fourier-transform spectrometers (FTS).

Two fundamental applications are studied: Integral Field Spectrographs (IFS) and Multi-Object Spectrographs (MOS). Integral field spectrographs provide contiguous coverage over a two-dimensional (usually square) field of view. On the other hand, a multiple object spectrograph can take advantage of the relatively low density and discreteness of the scene by only looking at a limited number and small parts of the entire (integral) FOV. By placing conveniently, i.e. on a line or a column (using fibres or other mechanisms), the pixels used for imaging, the remaining dimension of the detector array may be used for spectrometry. This makes for a very efficient use of all the available pixels.

4.2.1 Integral Field Spectrographs

This section compares the signal to noise ratio (SNR) of imaging spectrographs in different IFS configurations. This case is more general, i.e. it covers the measurement of the spectral content of all the pixels of an image. These results will be applied to the MOS.

4.2.1.1 Hypotheses

All configurations are compared using the same baseline. It consists in the complete measurement of the spectrum of an image, namely:

- an image consisting in K × L pixels;

- spectrum consisting in N resolved spectral bins of width $\Delta\sigma$ [cm^{-1}] (spectral resolution), extending from the low wavenumber σ_1 [cm^{-1}] to the high wavenumber σ_2 [cm^{-1}], for each pixel, so $N\Delta\sigma = \sigma_2-\sigma_1$;
- $\Phi_S(\sigma)$ is the count rate of the source per unit bandwidth [ph/sec/cm^{-1}];
- $\Phi_B(\sigma)$ is the count rate of the background per unit bandwidth [ph/sec/cm^{-1}], it is expressed in terms of the count rate of the scene $\Phi_B(\sigma) = \gamma\Phi_S(\sigma)$;
- measurement done in the same total duration time T [sec];
- each instrument configuration is assumed to have an efficiency $\eta_{instr}(\sigma)$ [—];
- average value of $\Phi_S(\sigma)$, $\Phi_B(\sigma)$ and $\eta_{instr}(\sigma)$ are used, Φ_S ,Φ_B and η_{instr}; and
- all instruments assumed to have the same throughput, otherwise the signal must be multiplied by the throughput).

Four noise contributions are considered:

1. photon noise from the source (PN);
2. photon noise from the background (BN);
3. detector noise (DN), spectrally white noise often associated with the dark current; and
4. read-out noise (RN).

The read-out noise differs from the detector noise in the sense that it does not depend on the measurement duration (or bandwidth). It is a constant value for each of the read-outs.

4.2.1.2 Tuneable filter

The tuneable filter (TF) instrument uses an optical bandpass filter such as a Fabry-Perot interferometer, or an acousto-optic tuneable filter. It could also be a multiple-filter instrument.

4.2.1.2.1 Characteristics

This configuration enables the measurement of the spectra of all the image pixels by using directly the K × L pixels of the focal plane array (FPA), and measuring alternatively the signal for each spectral bin, while the filter is tuned through each bandwidth to be covered. Common practices in the development of TF instruments make the bin spectral spacing smaller than the resolution, typically by a factor between 0.5 and 0.8. An overlap parameter is used to take into account the increased number of spectral bins needed to cover the full spectral range. Figure 16 shows the transmission curves of a typical TF for different overlap parameters.

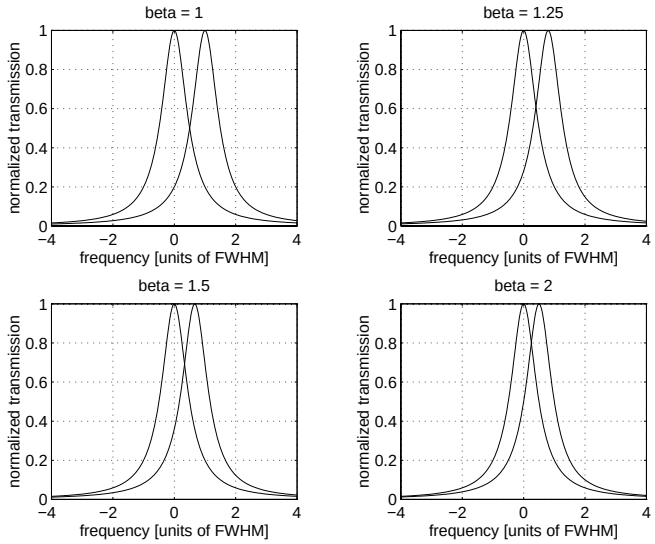

Figure 16 Transmission curves of typical tuneable filter (Fabry-Perot interferometer) for various overlap parameters.

Amongst TF instruments, Fabry-Perot interferometers are characterised by a constant full-width at half maximum (FWHM), so its resolving power varies with the frequency if a wide spectral range is to be covered. Moreover such filters have rather small spectral intervals, the so-called free spectral range (FSR), which limits the achievable spectral range. The FWHM is also proportional to the FSR through the finesse of the interferometer.

4.2.1.2.2 SNR performance

The signal available at each detector Q_{TF} [ph] is proportional to the bandwidth of the filter and to the duration of the measurement,

$$Q_{TF} = \eta_{TF}(\Phi_S + \Phi_B)\frac{\sigma_2 - \sigma_1}{\beta N}\frac{T}{\beta N}, \qquad (23)$$

where η_{TF} is the efficiency of the tuneable filter, Φ_S is the count rate of the scene, Φ_B is the count rate of the background, σ_1 and σ_2 are respectively the lower and the upper frequencies of the bandwidth to be covered, T is the total duration of the measurement (K × L spectra) and β is the overlap parameter.

The photon noise contribution [ph] is (Appendix A)

$$q_{TF_{PN}} = \sqrt{Q_{TF}}\ . \qquad (24)$$

The detector noise contribution [ph] is (Appendix A)

$$q_{TF_{DN}} = \sqrt{\frac{N_0}{2e^2}\frac{T}{\beta N}}, \qquad (25)$$

where N_0 is the level of the current noise power spectral density (single-sided) [A^2/Hz] at the entrance of the preamplifier, due to the detector and preamplifier resistors, and e stands for the elementary charge [C].

The read-out noise contribution [ph] is

$$q_{TF_{RN}} = n_R , \tag{26}$$

where n_R is the RMS value of the read-out noise.

The complete expression for the SNR for the tuneable filter is

$$SNR_{TF} = \frac{\eta_{TF}\Phi_S(\sigma_2 - \sigma_1)T}{\sqrt{\eta_{TF}(\Phi_S + \Phi_B)(\sigma_2 - \sigma_1)T\beta^2 N^2 + \frac{N_0 T}{2e^2}\beta^3 N^3 + n_R^2\beta^4 N^4}} . \tag{27}$$

Since all the pixels of the image are measured simultaneously, the SNR is independent of the size of the image.

4.2.1.3 Dispersive filter

The dispersive filter (TF) instrument is an optical spectrometer using a dispersive element such as a diffraction grating to spread spatially the spectrum.

4.2.1.3.1 Characteristics

This configuration enables the measurement of the spectra of the image by spreading spatially the spectrum of an image column over a K × N pixel FPA, and measuring alternatively the spectra for each column of the image, while the image is scanned across. Common practices in the development of DF instruments make the bin spectral spacing smaller than the resolution, typically by a factor between 0.5 and 0.8. An overlap parameter is used to take into account the increased number of spectral bins needed to cover the full spectral range. Figure 17 shows the transmission curves of a typical DF for different overlap parameters.

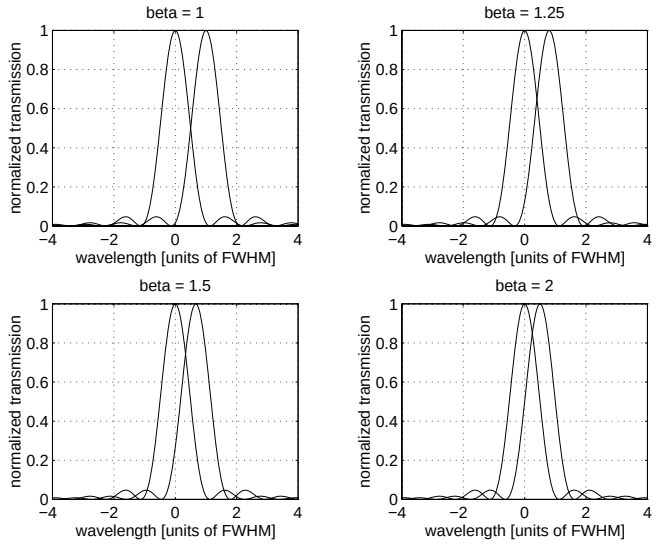

Figure 17 Transmission curves of typical dispersive filter (diffraction grating) for various overlap parameters.

Diffraction gratings are characterised by a constant resolving power in wavelength, so its resolving power varies with the frequency if a wide spectral range is to be covered. Moreover such filters have limited spectral range to octave bandwidth due to higher diffraction orders.

4.2.1.3.2 SNR performance

The signal available at each detector Q_{DF} [ph] is proportional to the bandwidth of the filter and to the duration of the measurement,

$$Q_{DF} = \eta_{DF}(\Phi_S + \Phi_B)\frac{\sigma_2 - \sigma_1}{\beta N}\frac{T}{L}, \tag{28}$$

where η_{DF} is the efficiency of the dispersive filter, Φ_S is the count rate of the scene, Φ_B is the count rate of the background, σ_1 and σ_2 are respectively the lower and the upper frequencies of the bandwidth to be covered, T is the total duration of the measurement (K × L spectra) and β is the overlap parameter.

The photon noise contribution [ph] is (Appendix A)

$$q_{DF_{PN}} = \sqrt{Q_{DF}}\,. \tag{29}$$

The detector noise contribution [ph] is (Appendix A)

$$q_{DF_{DN}} = \sqrt{\frac{N_0}{2e^2}\frac{T}{L}}, \tag{30}$$

where N_0 is the level of the current noise power spectral density (single-sided) [A^2/Hz] at the entrance of the preamplifier, due to the detector and preamplifier resistors, and e stands for the elementary charge [C].

The read-out noise contribution [ph] is

$$q_{DF_{RN}} = n_R, \tag{31}$$

where n_R is the RMS value of the read-out noise.

The complete expression for the SNR for the dispersive filter is

$$SNR_{DF} = \frac{\eta_{DF}\Phi_S(\sigma_2-\sigma_1)T}{\sqrt{\eta_{DF}(\Phi_S+\Phi_B)(\sigma_2-\sigma_1)T\beta NL + \frac{N_0 T}{2e^2}\beta^2 N^2 L + n_R^2\beta^2 N^2 L^2}}. \tag{32}$$

The SNR is strongly dependent of the size of the image.

4.2.1.4 Fourier-transform spectrometer

4.2.1.4.1 Characteristics

In contrast with tuneable and dispersive filters, Fourier-transform spectrometers (FTS) do not measure directly the spectrum. They measure the autocorrelation function of the scene, which is next Fourier-transformed to provide the spectrum. In its simplest form, the Fourier-transform spectrometer instrument is generally a variant of the Michelson interferometer. The autocorrelation function of the scene is measured as the optical path difference in the interferometer is swept. Two approaches are possible. Both sides of the so-called interferogram can be measured to improve the signal processing (double-sided interferogram, DSI), even if only one side (single-sided interferogram, SSI) is strictly needed because the autocorrelation is an even function. So Fourier-transform spectrometers use double-sided interferograms with M points (or single-sided interferograms with M/2 points) in order to achieve the measurement.

This configuration enables the measurement of the spectra of the image by using directly the K × L pixels of the FPA, and measuring alternatively the signal for each optical path difference, while one arm of the interferometer is lengthened / shortened with regard to the other.

4.2.1.4.2 SNR performance

The average signal available at each detector Q_{FTS} [ph] is proportional to the full bandwidth covered by the instrument and to the duration of the measurement,

$$Q_{FTS} = \eta_{FTS}(\Phi_S+\Phi_B)(\sigma_2-\sigma_1)\frac{T}{M\alpha/2}, \tag{33}$$

where η_{FTS} is the efficiency of the spectrometer, Φ_S is the count rate of the scene, Φ_B is the count rate of the background, σ_1 and σ_2 are respectively the lower and the upper frequencies of the bandwidth to be covered, T is the total duration of the measurement (K × L spectra), M is the number

of points of the double-sided interferogram, and α is a parameter which equals 2 for DSI instrument and 1 for SSI instrument.

It is common to understand the FTS as an instrument sending half the signal to the second port, the latter being transmission to a distinct port or reflection back to the scene depending on the particular design. However a close look at the instrument physical principles shows the need to modulate the signal spectrum in order to obtain an interferogram (the interferometer is often called a modulator). The best performance achievable is a 100% modulation, i.e. an interferogram having all the signal at zero path difference (ZPD) and half the signal at maximum OPD (e.g. see Figure 30). Once the Fourier transform is applied to the interferogram, it is seen that half the signal is unmodulated, so it is in the DC component. Meanwhile the other half of the signal is modulated and is located at Fourier frequencies that will be matched to optical frequencies through the sampling frequency and the sweeping velocity. From this modulated part, half of the signal is in the negative frequencies and half is located in the positive frequencies. Therefore the maximum theoretical efficiency of a single port FTS is ½. Dual port devices can be used at the price of doubling the detector hardware.

SSI instruments have twice the integration time per sample for each of their interferogram points, since they have 2 times less points to measure in the same time interval. This results in a factor 2 improvement on the signal side. However other considerations, such as the more difficult calibration procedures, decrease this apparent sensitivity advantage.

To properly sample the interferogram (to satisfy the Nyquist criterion), the number of points of the DSI must exceed two times the ratio of the highest frequency to the spectral resolution,

$$M \geq 2\frac{\sigma_2}{\Delta\sigma} \geq 2\frac{\sigma_2 - \sigma_1}{\Delta\sigma} = 2N\,, \tag{34}$$

which is itself always larger than two times the number of spectral bins. In common practice, some margin is kept between Nyquist rate (half of sampling frequency) and maximum frequency σ_2.

The photon noise contribution [ph] is (Appendix A)

$$q_{FTS_{PN}} = \sqrt{Q_{FTS}}\,. \tag{35}$$

The detector noise contribution [ph] is (Appendix A)

$$q_{FTS_{DN}} = \sqrt{\frac{N_0}{2e^2}\frac{T}{M\alpha/2}}\,, \tag{36}$$

where N_0 is the level of the current noise power spectral density (single-sided) [A^2/Hz] at the entrance of the preamplifier, due to the detector and preamplifier resistors, and e stands for the elementary charge [C].

The read-out noise contribution [ph] is

$$q_{FTS_{RN}} = n_R\,, \tag{37}$$

where n_R is the RMS value of the read-out noise.

The complete expression for the SNR in the interferogram domain is

$$SNR_{FTS_{IGM}} = \frac{\eta_{FTS}(\Phi_S + \Phi_B)(\sigma_2 - \sigma_1)T}{\sqrt{\eta_{FTS}(\Phi_S + \Phi_B)(\sigma_2 - \sigma_1)T\frac{M\alpha}{2} + \frac{N_0}{2e^2}T\frac{M\alpha}{2} + n_R^2\frac{M^2\alpha^2}{4}}}. \quad (38)$$

The SNR in the spectrum and in the interferogram domains are related by the following coefficient (see Appendix B)

$$SNR_{FTS} = \frac{1}{N}\sqrt{\frac{M\alpha/2}{2}}SNR_{FTS_{IGM}}. \quad (39)$$

This last factor takes into account the facts that the total power of the noise samples in the interferogram domain is split in 2 over the negative and positive frequencies and it is also split in 2 over the real and imaginary parts of the spectrum. The latter is a benefit only for double-sided interferograms, since the imaginary part of the spectrum is related directly to the odd part of the noise samples. For SSI, the noise is mirrored, as the signal, so it ends completely in the real part of the spectrum. Moreover the noise power is spread equally over all the frequencies. Since only the positive frequency content of the real part of the spectrum is kept, while the signal is spread over N spectral bins, the factor becomes that of Equation 39.

Thus the complete expression for the SNR for the Fourier-transform spectrometer is

$$SNR_{FTS} = \frac{\eta_{FTS}\Phi_S(\sigma_2 - \sigma_1)T}{\sqrt{2\eta_{FTS}(\Phi_S + \Phi_B)(\sigma_2 - \sigma_1)TN^2 + N_0TN^2 + \alpha n_R^2 MN^2}}, \quad (40)$$

where α is a parameter equal to 2 for double-sided interferograms and it equals 1 for single-sided interferograms. The only difference in SNR performance between DSI and SSI FTS' is the ultimate SNR achieved for read-out noise limited measurements, where SSI dominates by a factor $\sqrt{2}$. So, for most practical cases, they both have the same performance.

SSI instruments are swept at half speed of DSI ones, so the measured interferogram samples are 2 times larger. However SSI instruments take all the noise to the real part of the spectrum, thus resulting in a improvement by a factor $\sqrt{2}$. The latter disappears for photon and detector noises since the noise contributions are also higher by a factor $\sqrt{2}$.

Since all the pixels of the image are measured simultaneously, the SNR is independent of the size of the image.

4.2.1.5 Summary

Table 3 gives a summary of the SNR behaviours for the various configurations and noises. Also listed in Table 3 are other important parameters to be considered to compare the instruments, along with the SNR, namely

- the size of the necessary focal-plane array (FPA);
- the duration of each sample measurement (giving the speed needed for the FPA); and

- the maximum signal level (to be compared with the dark current and the detector saturation levels).

Table 3: Summary of SNR in the photon noise limit (PN), detector noise limit (DN) and the readout noise limit (RN) for the various instruments (TF: tuneable filter; DF: dispersive filter; FTS: Fourier-transform spectrometer (α=2: double-sided interferogram; α=1: single-sided interferogram)

Type	*FPA*	*Sample Duration*	*Maximum Signal*	*SNR-PN*	*SNR-DN*	*SNR-RN*
TF	$K \times L$	$\Delta t \frac{1}{\beta N}$	$Q_0 \frac{\eta_{TF}}{\beta^2 N^2}$	$SNR_{\max_{PN}} \frac{\sqrt{\eta_{TF}}}{\beta N}$	$SNR_{\max_{DN}} \frac{\eta_{TF}}{\beta N \sqrt{\beta N}}$	$SNR_{\max_{RN}} \frac{\eta_{TF}}{\beta^2 N^2}$
DF	$K \times \beta N$	$\Delta t \frac{1}{L}$	$Q_0 \frac{\eta_{DF}}{\beta N L}$	$SNR_{\max_{PN}} \frac{\sqrt{\eta_{DF}}}{\sqrt{\beta N L}}$	$SNR_{\max_{DN}} \frac{\eta_{DF}}{\beta N \sqrt{L}}$	$SNR_{\max_{RN}} \frac{\eta_{DF}}{\beta N L}$
FTS	$K \times L$	$\Delta t \frac{1}{M}$	$Q_0 \frac{\eta_{FTS}}{M}$	$SNR_{\max_{PN}} \frac{\sqrt{\eta_{FTS}}}{\sqrt{2N}}$	$SNR_{\max_{DN}} \frac{\eta_{FTS}}{\sqrt{2}N}$	$SNR_{\max_{RN}} \frac{\eta_{FTS}}{\sqrt{\alpha} N \sqrt{M}}$

In Table 3, the following definition was used

$$Q_o = \Phi_S (\sigma_2 - \sigma_1) T \, . \tag{41}$$

The maximum SNRs are given in Table 4 for each noise contribution.

Table 4: Maximum SNR for each of the noise limits

Photon Noise (scene / background)	*Detector Noise*	*Read-out Noise*
$SNR_{\max_{PN}} = \sqrt{\frac{\Phi_S (\sigma_2 - \sigma_1) T}{1+\gamma}}$	$SNR_{\max_{DN}} = \Phi_S (\sigma_2 - \sigma_1) \sqrt{\frac{2e^2 T}{N_0}}$	$SNR_{\max_{RN}} = \frac{\Phi_S (\sigma_2 - \sigma_1) T}{n_R}$

4.2.1.5.1 Summary for N^3 data cube

In order to compare the instruments for integral field applications, we make comparisons for images with N × N pixels, each having N resolved spectral bins. Thus TF and FTS need a FPA with N × N pixels, while the DF still need a larger FPA. This situation makes full use of the available detectors.

Table 5: Summary of SNR in the photon noise limit (PN), detector noise limit (DN) and the readout noise limit (RN) for the various instruments for integral field applications (TF: tuneable

filter; DF: dispersive filter; FTS: Fourier-transform spectrometer (α=2: double-sided interferogram; α=1: single-sided interferogram)

Type	*FPA*	*Sample Duration*	*Maximum Signal*	*SNR-PN*	*SNR-DN*	*SNR-RN*
TF	$N \times N$	$\Delta t \frac{1}{\beta N}$	$Q_0 \frac{\eta_{TF}}{\beta^2 N^2}$	$SNR_{\max_{PN}} \frac{\sqrt{\eta_{TF}}}{\beta N}$	$SNR_{\max_{DN}} \frac{\eta_{TF}}{\beta N \sqrt{\beta N}}$	$SNR_{\max_{RN}} \frac{\eta_{TF}}{\beta^2 N^2}$
DF	$N \times \beta N$	$\Delta t \frac{1}{N}$	$Q_0 \frac{\eta_{DF}}{\beta N^2}$	$SNR_{\max_{PN}} \frac{\sqrt{\eta_{DF}}}{\sqrt{\beta} N}$	$SNR_{\max_{DN}} \frac{\eta_{DF}}{\beta N \sqrt{N}}$	$SNR_{\max_{RN}} \frac{\eta_{DF}}{\beta N^2}$
FTS	$N \times N$	$\Delta t \frac{1}{M}$	$Q_0 \frac{\eta_{FTS}}{M}$	$SNR_{\max_{PN}} \frac{\sqrt{\eta_{FTS}}}{\sqrt{2} N}$	$SNR_{\max_{DN}} \frac{\eta_{FTS}}{\sqrt{2} N}$	$SNR_{\max_{RN}} \frac{\eta_{FTS}}{\sqrt{\alpha} N \sqrt{M}}$

Framed formulae correspond to typical situations encountered in practice. Because all these instruments cannot reach the same throughput, FTS ones have much higher signal levels and they tend to be more PN limited, whereas TF / DF tend to be more DN / RN limited. It is shown that the different approaches have very different behaviours, when one considers only SNR. FTS appears to be superior for higher spectral resolution imaging applications. Nevertheless a complete numerical evaluation of the SNR, considering simultaneously all the contributions, needs to be done in order to compare the levels achievable with each instrument.

The SNR performance is compared for each of the noise contributions: photon noise (see Figure 18), detector noise (see Figure 19) and read-out noise (see Figure 20).

Figure 18 presents the variation of the SNR with an increase of the number of spectral bins, which corresponds mainly to an increased resolution. For photon noise limited, all instrument types behave about equally, the dispersive filter having a small advantage.

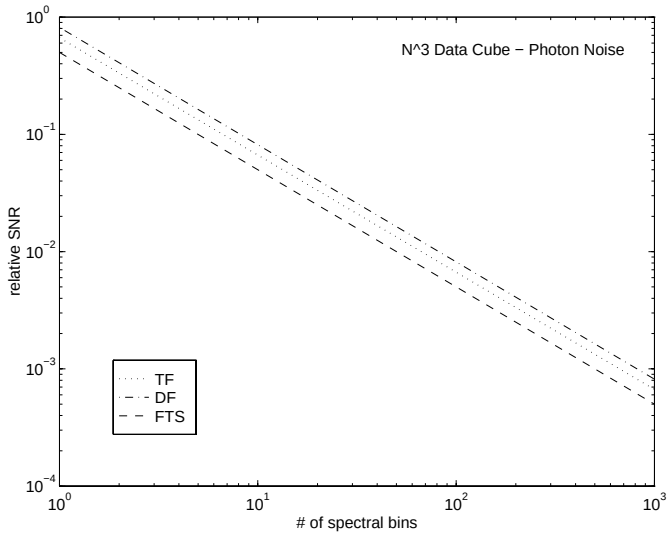

Figure 18 SNR for photon noise limited instruments in integral field applications.

Figure 19 presents the variation of the SNR with an increase of the number of spectral bins, which corresponds mainly to an increased resolution. For detector noise limited, the FTS has a clear advantage (the so-called multiplex advantage) over the other types of instrument.

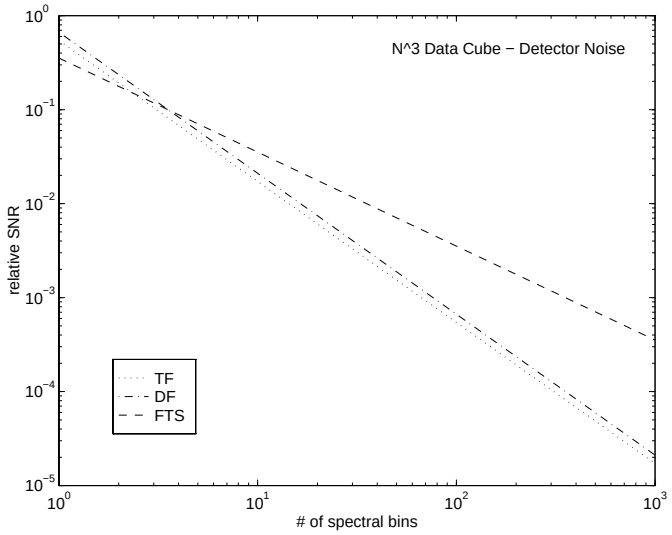

Figure 19 SNR for detector noise limited instruments in integral field applications.

Figure 20 presents the variation of the SNR with an increase of the number of spectral bins, which corresponds mainly to an increased resolution. For read-out noise limited, the FTS has still a clear advantage (the so-called multiplex advantage) over the other types of instrument. SSI instruments have a slight advantage over DSI.

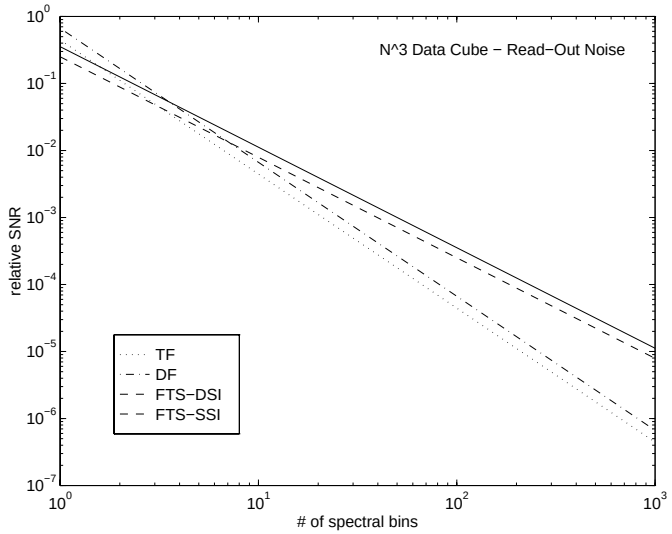

Figure 20 SNR for read-out noise limited instruments in integral field applications.

4.2.1.5.2 Summary for single pixel

In order to compare the instruments for multiple object applications, we make comparisons for images with 1 × 1 pixel, having N resolved spectral bins. Thus each instrument type uses as many detectors as needed, expecting them to be available.

Table 6: Summary of SNR in the photon noise limit (PN), detector noise limit (DN) and the readout noise limit (RN) for the various instruments for multiple object applications (TF: tuneable filter; DF: dispersive filter; FTS: Fourier-transform spectrometer (α=2: double-sided interferogram; α=1: single-sided interferogram)

Type	*FPA*	*Sample Duration*	*Maximum Signal*	*SNR-PN*	*SNR-DN*	*SNR-RN*
TF	1×1	$\Delta t \frac{1}{\beta N}$	$Q_0 \frac{\eta_{TF}}{\beta^2 N^2}$	$SNR_{\max_{PN}} \frac{\sqrt{\eta_{TF}}}{\beta N}$	$SNR_{\max_{DN}} \frac{\eta_{TF}}{\beta N\sqrt{\beta N}}$	$SNR_{\max_{RN}} \frac{\eta_{TF}}{\beta^2 N^2}$
DF	$1\times \beta N$	Δt	$Q_0 \frac{\eta_{DF}}{\beta N}$	$SNR_{\max_{PN}} \frac{\sqrt{\eta_{DF}}}{\sqrt{\beta N}}$	$SNR_{\max_{DN}} \frac{\eta_{DF}}{\beta N}$	$SNR_{\max_{RN}} \frac{\eta_{DF}}{\beta N}$
FTS	1×1	$\Delta t \frac{1}{M}$	$Q_0 \frac{\eta_{FTS}}{M}$	$SNR_{\max_{PN}} \frac{\sqrt{\eta_{FTS}}}{\sqrt{2N}}$	$SNR_{\max_{DN}} \frac{\eta_{FTS}}{\sqrt{2}N}$	$SNR_{\max_{RN}} \frac{\eta_{FTS}}{\sqrt{\alpha}N\sqrt{M}}$

Framed formulae correspond to typical situations encountered in practice. Because all these instruments cannot reach the same throughput, FTS ones have much higher signal levels and they tend to be more PN limited, whereas TF / DF tend to be more DN / RN limited. It is shown that the different approaches have relatively similar behaviour, when one considers only SNR for single pixel applications. Nevertheless a complete numerical evaluation of the SNR, considering simultaneously all the contributions, needs to be done in order to compare the levels achievable with each instrument.

Since it needs many detectors to be efficient, DF is taking advantage of the numerous detectors available. This is not the case for the TF / FTS. TF and FTS achieve the same SNR for a N^3 data cube or for a single pixel.

The SNR performance is compared for each of the noise contributions: photon noise (see Figure 21), detector noise (see Figure 22) and read-out noise (see Figure 23).

Figure 21 gives the variation of the SNR with an increase of the number of spectral bins, which corresponds mainly to an increased resolution. For photon noise limited, the DF has still a clear advantage (taking benefit of the extraneous detectors available) over the other types of instrument.

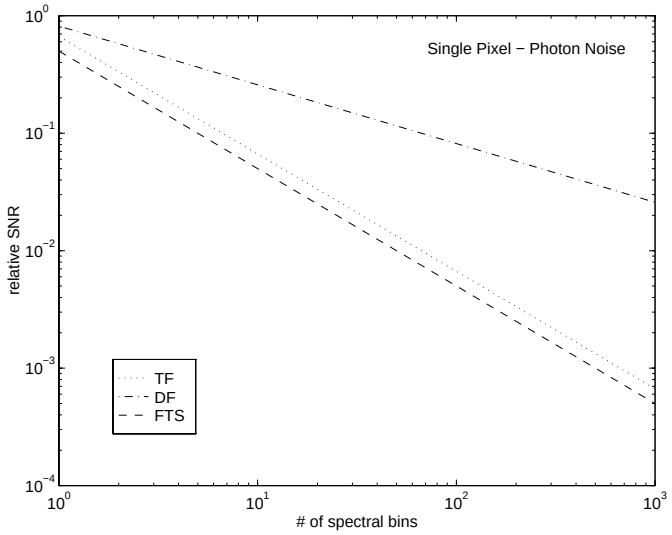

Figure 21 SNR for photon noise limited instruments in multiple object applications.

Figure 22 gives the variation of the SNR with an increase of the number of spectral bins, which corresponds mainly to an increased resolution. For detector noise limited, the DF and FTS have a net advantage over the TF instrument. DF achieves slightly higher SNR than FTS, at the cost of using many detectors.

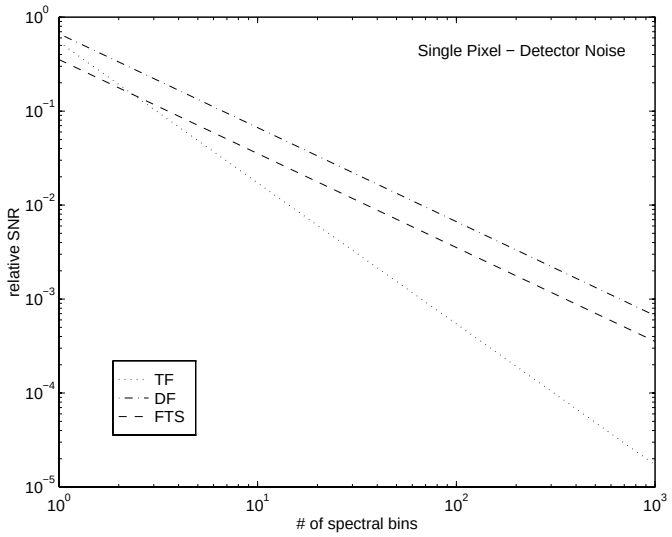

Figure 22 SNR for detector noise limited instruments in multiple object applications.

Figure 23 gives the variation of the SNR with an increase of the number of spectral bins, which corresponds mainly to an increased resolution. For read-out noise limited, the DF has the best sensitivity (taking benefit of the extraneous detectors available).

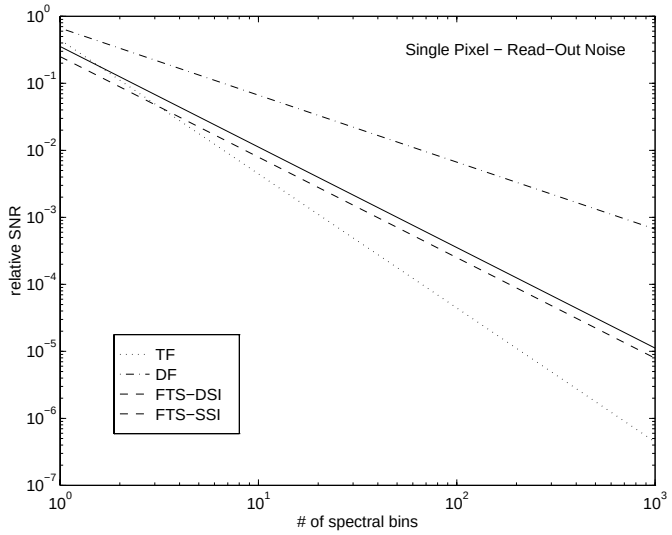

Figure 23 SNR for read-out noise limited instruments in multiple object applications.

4.2.2 Multi-Object Spectrographs

All the results of Section 4.2.1 can be applied directly to the case of multi-object spectrograph, by simply replacing L by 1. This has been done in Section 4.2.1.5.2.

In this case, the dispersive spectrometer enjoys a relative improvement due to the fact that it uses a multi-detector group (that provide the spectral information along the dispersion axis) for each of the object in the field, as opposed to the other instruments that only use one pixel to build the spectrum (using time modulation).

5. IFTS SWEEP STRATEGIES

5.1 INTRODUCTION

This section analyses various approaches for optimising the sensitivity of the IFTS. The main motivation is to investigate means of making the FTS more attractive, because it is believed to have sensitivity disadvantage as compared to dispersive spectrometers. Please refer to Sections 2 and 4 for more details on the sensitivity calculations.

5.2 PROPOSED METHODS

5.2.1 Uneven integration time versus OPD

It has been suggested by a number of people that using a uneven integration time versus OPD may be a way to improve the signal-to-noise ratio of a FTS measurement. The idea is to spend more time in some area of the optical path difference in order to locally improve the noise in that section of the interferogram. This is illustrated in Figure 24 where we consider a step-scan FTS equipped with an integrating detector for simplicity. Similar discussions can be held for a rapid-scan FTS equipped with an AC-coupled, band-limited detector. The most "natural" way to perform the interferogram samples is to use equal integration time for all OPD samples (dash line). However we would like to investigate the efficiency of uneven integration times such as the example shown in Figure 24 (solid line).

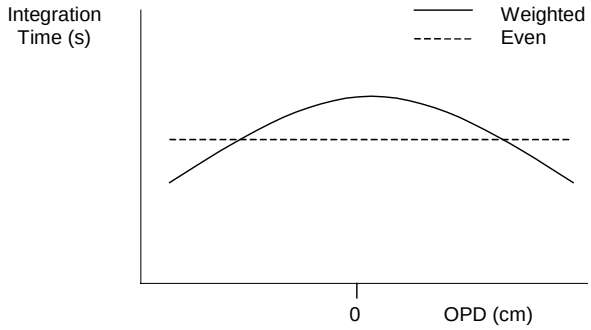

Figure 24 Integration time schemes

In order to derive some quantitative comparison, let us define the following terms. Let

T be the total integration time

N be the total number of interferogram (IGM) samples

τ_i be the integration time on IGM sample i, with $i = 0$ *to* $N-1$

so that the total time is

$$T = \sum_{i=0}^{N-1} \tau_i \tag{42}$$

If the integration time is constant along the OPD we have

$$T = \sum_{i=0}^{N-1} \tau_i = \sum_{i=0}^{N-1} \bar{\tau} = N\bar{\tau} \tag{43}$$

With $\bar{\tau}$ the constant integration time for each sample

On the other hand for uneven integration times τ_i' defined as $\tau_i' = \rho_i \bar{\tau}$, where ρ_i are positive numbers we have

$$T = N\ \bar{\tau} = \sum_{i=0}^{N-1} \tau_i' = \sum_{i=0}^{N-1} \rho_i\ \bar{\tau} = \bar{\tau} \sum_{i=0}^{N-1} \rho_i \tag{44}$$

which implies that

$$\sum_{i=0}^{N-1} \rho_i\ = N \tag{45}$$

We will now analyse the problem by separating the noise ε_x from the signal S_x in the interferogram, as illustrated in Figure 25.

$$IGM = S_x + \varepsilon_x \tag{46}$$

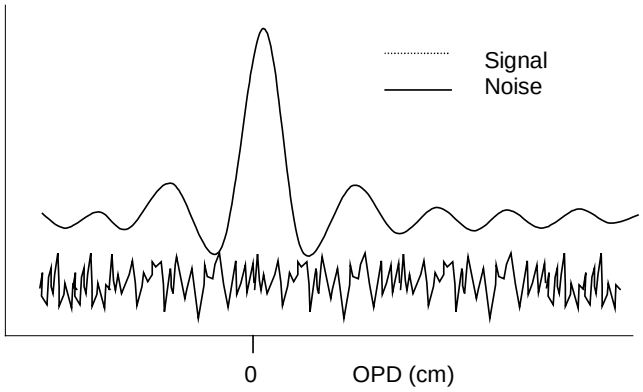

Figure 25 Decomposing the interferogram in signal and noise

Of course the end goal is to obtain the optimum SNR in the spectral domain, where we can also separate the signal and the noise in a similar manner.

$$SPC = S_\sigma + \varepsilon_\sigma \tag{47}$$

Because of the linearity of the Fourier transform we can consider that the signal in the spectral domain is the FT of the signal in the interferogram domain; $S_\sigma = \Im[S_x]$ and correspondingly that the noise in the spectral domain is the FT of the noise in the interferogram domain; $\varepsilon_\sigma = \Im[\varepsilon_x]$.

We will now consider the case illustrated in Figure 26. This figure considers two cases: a) a "classical" constant integration time and b) a triangular integration time such that the total time is equal for both cases. In the first case we obtain in c) a generic-looking interferogram signal and noise. Strictly speaking the example illustrated in Figure 26 would be either detector dark noise or readout noise dominated rather than photon noise dominated, because of the uniform noise amplitude across the OPD. However the mathematical development presented here does not assume or require OPD-independent noise and is general (applicable to photon noise for example). Separate Fourier Transform of the signal and noise yield the spectral signal and noise as shown in d).

With a weighted integration time illustrated in b) we get the distorted signal and noise as shown in e). With this triangular weighting the signal is increased around Zero Path Difference (ZPD) and decreased at the OPD extremities, both linearly with integration time. The noise on the other hand varies with the square root of the integration time, whether the noise is due to photon noise or dark noise. This is graphically represented in e).

In order to perform a equitable comparison between the weighted versus constant integration time case, one must normalize the signal and noise of the former case. If this is not done, the spectral signal would correspond to numerically apodizing the interferogram, and the spectral resolution would be affected. Changing the spectral resolution clearly has an effect on the SNR as explained in Section 5.2.2. In this section we want to study the effect of changing the integration times alone for a constant spectral resolution so we want to remove the apodization of the signal. This is shown in Figure 26 f) where both the signal and noise have been divided by the integration time profile as shown in b). This as the effect of making the signal equal to the even integration time case b). This also has the effect of changing the noise distribution as shown in f). The noise thus has a global scaling inversely proportional to the square root of the integration time. Once transformed to the spectral domain, the noise appear white g) but it is not because it is now affected by a degree of correlation. This arises because the noise in g) is really the white noise of d) convolved with the Fourier Transform of the envelope function that relates the noise in f) as compared to the noise in c).

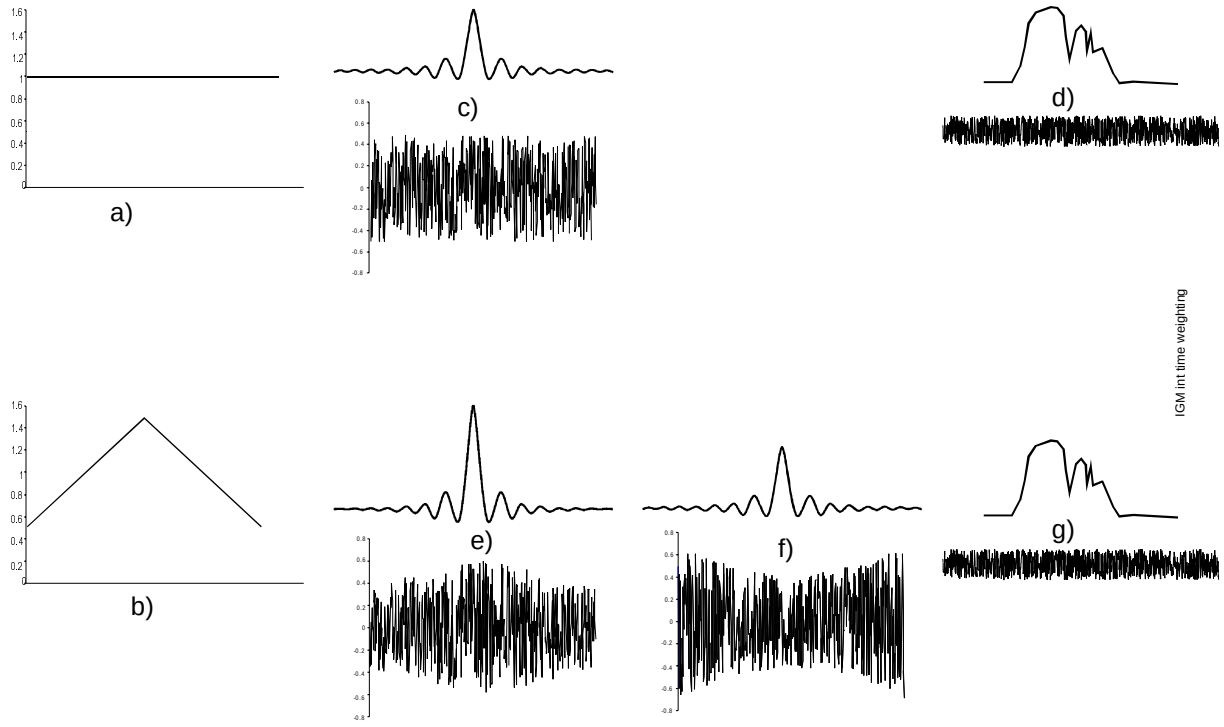

Figure 26 Comparison of even and uneven integration time approaches

To estimate the increase or decrease of the amplitude of noise for the weighted integration time case, we will use the formulation of Parseval's theorem given in Equation 48.

$$\langle \varepsilon_\sigma \rangle = \sqrt{\frac{\Delta x}{\Delta \sigma}} \langle \varepsilon_x \rangle \tag{48}$$

where Δx is the maximum path difference (cm)

$\Delta\sigma$ is half the sampling frequency (cm^{-1})

$\langle\ \rangle$ is the standard deviation operator applied to the vector, respectively in the spectral or interferogram domain.

Since Δx and $\Delta\sigma$ are constant for both the constant (superscript c) and weighted (superscript w) integration time cases, we can write

$$\frac{\langle \varepsilon_\sigma^w \rangle}{\langle \varepsilon_\sigma^c \rangle} = \frac{\langle \varepsilon_x^w \rangle}{\langle \varepsilon_x^c \rangle} \tag{49}$$

Following the explanations describing Figure 26 we can also write that on a small portion OP of the OPD,

$$\left\langle \varepsilon_x^w \right\rangle_{OP} = \frac{\left\langle \varepsilon_x^c \right\rangle_{OP}}{\sqrt{\rho_i}} \tag{50}$$

Equation 50 can be reasoned as follows, on a small portion of the OPD where the integration time can be considered constant for a smooth and slowly changing weighting function, the noise in the weighted integration time case is simply inversely proportional to the ratio of the integration time ρ_i . Equation 50 also makes the assumption of ergoticity, i.e. that the amplitude of the noise is the same statistically (for example for several experiments) or for neighbouring points in the vector in the spectral or interferogram domain.

Using Equation 50, Equation 49 can be rewritten as

$$\frac{\left\langle \varepsilon_\sigma^w \right\rangle}{\left\langle \varepsilon_\sigma^c \right\rangle} = \frac{\sqrt{\frac{1}{N}\sum_{wholeOPD}\left(\varepsilon_x^w\right)^2}}{\left\langle \varepsilon_x^c \right\rangle} = \frac{\sqrt{\frac{1}{N}\sum_{OP1}\left(\varepsilon_x^w\right)^2 + \frac{1}{N}\sum_{OP2}\left(\varepsilon_x^w\right)^2 + \frac{1}{N}\sum_{OP3}\left(\varepsilon_x^w\right)^2 + \ldots}}{\left\langle \varepsilon_x^c \right\rangle}$$

$$\frac{\sqrt{\left\langle \varepsilon_\sigma^w \right\rangle_{OP1}^2 + \left\langle \varepsilon_\sigma^w \right\rangle_{OP2}^2 + \left\langle \varepsilon_\sigma^w \right\rangle_{OP3}^2 + \ldots}}{\sqrt{\left\langle \varepsilon_\sigma^c \right\rangle_{OP1}^2 + \left\langle \varepsilon_\sigma^c \right\rangle_{OP2}^2 + \left\langle \varepsilon_\sigma^c \right\rangle_{OP3}^2 + \ldots}} = \frac{\sqrt{\frac{1}{\rho_{OP1}}\left\langle \varepsilon_\sigma^c \right\rangle_{OP1}^2 + \frac{1}{\rho_{OP2}}\left\langle \varepsilon_\sigma^c \right\rangle_{OP2}^2 + \frac{1}{\rho_{OP3}}\left\langle \varepsilon_\sigma^c \right\rangle_{OP3}^2 + \ldots}}{\sqrt{\left\langle \varepsilon_\sigma^c \right\rangle_{OP1}^2 + \left\langle \varepsilon_\sigma^c \right\rangle_{OP2}^2 + \left\langle \varepsilon_\sigma^c \right\rangle_{OP3}^2 + \ldots}} \tag{51}$$

It can be shown that Equation 51 is always > 1.

This means that the noise (standard deviation) in any weighted approach is larger or at best equal to the noise in a constant integration time approach. This shows that in general the weighted approach is worse than using the usual constant integration time approach and that it does not constitute an obvious candidate for improving the SNR of an FTS measurement.

This however does not mean that there is no value in using a weighted approach. Apart from increasing the total noise, a weighted approach will "colour" the noise so that it is possible to favor low frequency or high frequency noise, in a manner decoupled from the signal itself (which is usually treated by performing numerical apodization). In other words it provides a extra degree of liberty in signal processing, allowing to treat the noise separately from the signal. If a particular science application is highly dependent on a particular type of noise, it is conceivable to use the weighted integration time approach to reduce this type of noise at the detriment of another type of noise. This judgement however is beyond the scope of this study.

5.2.2 Optimization of OPD and Numerical Apodization

The figure of merit commonly used for the sensitivity of spectroradiometer is the Noise Equivalent Spectral Radiance (NESR).

$$NESR(\sigma) = \frac{I_N(\sigma)}{R_{AC}(\sigma)\tau(\sigma)M(\sigma)\Theta\sqrt{t}\Delta\sigma\ F} \qquad (52)$$

where $I_N(\sigma)$ is the noise current (A $Hz^{-1/2}$)

$R_{AC}(\sigma)$ is the detector responsivity (A W^{-1})

$\tau(\sigma)$ is the system transmission ()

$M(\sigma)$ is the system modulation ()

Θ is the system Étendue (sr cm^2)

t is the acquisition time (s)

$\Delta\sigma$ is the spectral interval (cm^{-1}) = 1/(2MPD)

F is a factor dependant on the numerical apodization factor

According Equation 52, with everything else being constant, the NESR is inversely proportional to the spectral resolution. The spectral interval $\Delta\sigma$ is directly related to the spectral resolution[1] and simply the inverse of twice the maximum OPD (MPD). The factor *F* is a number larger than 1 for most numerical apodization functions. It is easy to see that the noise in the spectrum will be decreased if the noise in the interferogram is decreased by a numerical apodization function (see Equation 50).

From Equation 52, we see that one can reduce the noise in the spectrum by reducing MPD and/or performing numerical apodization on the interferogram. However both of these methods lead to a decrease of spectral resolution or information. This behaviour is expected of all spectrometers in general and not only of FTS.

For all missions, there should be a trade study performed to find the optimum spectral resolution to achieve the maximum science by trading noise and spectral resolution.

[1] The term spectral resolution is ill defined. Several definitions exist and tend to vary from one scientific domain to the other.

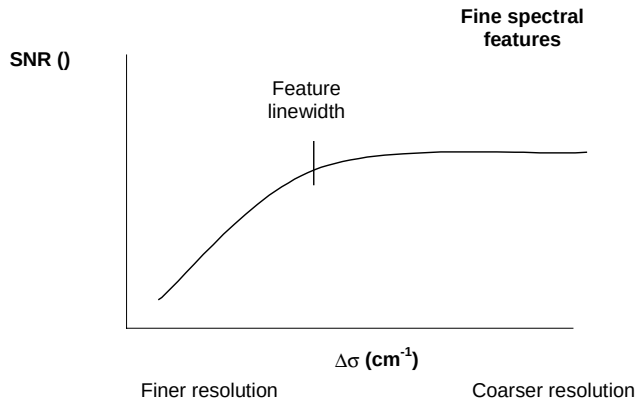

Figure 27 SNR versus Spectral Interval

Figure 27 shows the behaviour of the SNR of fine spectral features. The left side of Figure 27 illustrates the statement that the SNR decreases when the spectral resolution is decreased. This holds when the spectral resolution is better than the spectral feature, i.e. when the feature is resolved. If the feature is not resolved, the data points at the peak of the feature will decrease linearly with the spectral resolution, offsetting any reduction of noise, leading to a constant SNR. This underlines the fact that Equation 52 considers only the noise and not the possible change of signal, so it holds for spectrally resolved features.

6. APPENDIX A: NOISE CONTRIBUTIONS

This section describes the noise processes present in photon counting experiments, namely shot noise and additive white noise.

6.1 SHOT NOISE IN A PHOTON COUNTING PROCESS

In this appendix, photon counting is studied as a random process such that the photons produce the following current:

$$n(t) = \sum_i e\delta(t - t_i), \tag{53}$$

where e is the electron charge and t_i are the random instants of arrival of photons which is known to follow a Poisson distribution [PAP91]. The mean arrival rate is:

$$\lambda = (\Phi_S + \Phi_B)(\sigma_2 - \sigma_1) = \frac{I_0}{e}. \tag{54}$$

The expectation value of n(t) can then be evaluated:

$$E\{n(t)\} = \lambda e = I_0. \tag{55}$$

The autocorrelation function and the doubled-sided power spectral density of n(t) are respectively:

$$R_n(\tau) = e^2\lambda^2 + e^2\lambda\delta(t) \tag{56}$$

and

$$S_n(f) = e^2\lambda^2\delta(f) + e^2\lambda. \tag{57}$$

Now, the process n(t) is altered in some way by the detector. Let $n_f(t)$ be the detected process and let define $n_f(t)$ so that:

$$n_f(t) = h(t) \otimes n(t), \tag{58}$$

where h(t) is the impulse response of the detector and $\otimes$ stands for the convolution. The expectation and variance of $n_f(t)$ are accordingly:

$$E\{n_f(t)\} = e\lambda \int_{-\infty}^{\infty} h(t)dt \tag{59}$$

and

$$\sigma_{n_f}^2 = e^2\lambda \int_{-\infty}^{\infty} h^2(t)dt. \tag{60}$$

6.2 CHARGE-ACCUMULATING DETECTION

6.2.1 Shot noise

If the detector is accumulating charges, such as a CCD, the function h(t) is a unitary boxcar of duration Δt, that is $h(t)=u(t)-u(t-\Delta t)$ (see Figure 28).

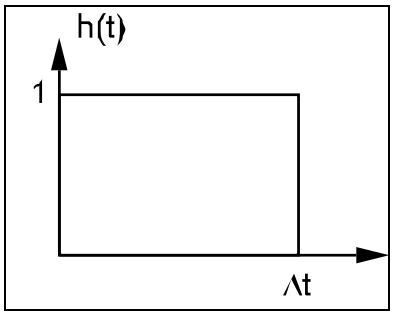

Figure 28 Impulse function of a charge-accumulating detector

The expectation and variance of $n_f(t)$ are in this case:

$$E\{n_f(t)\} = e\lambda\Delta t = I_0\Delta t = Q_0 \tag{61}$$

and

$$\sigma_{n_f}^2 = e^2\lambda\Delta t = eI_0\Delta t = eQ_0 . \tag{62}$$

The signal to noise ratio can finally be calculated:

$$SNR = \frac{e\lambda\Delta t}{\sqrt{e^2\lambda\Delta t}} = \sqrt{\lambda\Delta t} . \tag{63}$$

This result shows that the signal to noise is the square root of the average number of photons detected in the time interval Δt, as it is expected for standard photon counting experiment.

6.2.2 Additive white noise

If the system is limited by a constant single-sided white noise level N_0 (in A^2/Hz), the noise variance would instead be:

$$\sigma_{n_f}^2 = \frac{N_0}{2}\Delta t . \tag{64}$$

6.3 PHOTOCURRENT DETECTION

6.3.1 Shot noise

For a photocurrent detector followed by a normalised electrical integrator, the impulse response is a unitary area boxcar of duration Δt.

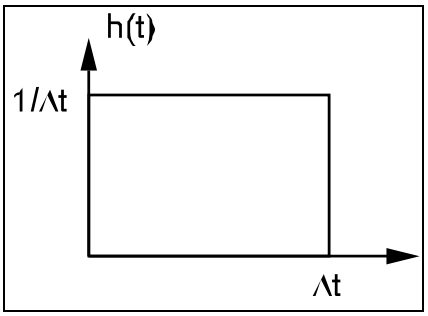

Figure 29 Impulse response of a photocurrent detector followed by a normalised integrator.

Here h(t) = (u(t)-u(t-Δt))/Δt. The expectation and variance of $n_f(t)$ are in that case:

$$E\{n_f(t)\} = e\lambda = I_0 \tag{65}$$

and

$$\sigma_{n_f}^2 = \frac{e^2\lambda}{\Delta t} = \frac{eI_0}{\Delta t}. \tag{66}$$

The signal to noise ratio can finally be calculated:

$$SNR = \frac{e\lambda}{\sqrt{e^2\lambda/\Delta t}} = \sqrt{\lambda \Delta t}. \tag{67}$$

This result shows that the signal to noise ratio is the same for both detector types.

6.3.2 Additive white noise

If the system is limited by a constant single-sided white noise level N_0 (in A^2/Hz), the noise variance would instead be:

$$\sigma_{n_f}^2 = \frac{N_o}{2}\frac{1}{\Delta t}. \tag{68}$$

7. APPENDIX B: EFFECT OF A DISCRETE FOURIER TRANSFORMATION ON SNR

The aim of this appendix is to establish the effects on the signal to noise ratio when applying a discrete Fourier transformation (DFT) on a temporal signal. The goal is to be able to deduce to spectral signal to noise ratio for a given value of the SNR on a time signal.

7.1 DOUBLE-SIDED INTERFEROGRAMS

Let's start with a widely used definition of the DFT, its inverse and the discrete Parseval theorem for a real signal of length M [OPP89]:

$$DFT: X[k] = \sum_{n=0}^{M-1} x[n] e^{j2\pi \frac{k}{M} n}, \tag{69}$$

$$DFT^{-1}: x[n] = \frac{1}{M} \sum_{k=0}^{M-1} X[k] e^{-j2\pi \frac{k}{M} n} \tag{70}$$

and

$$\sum_{n=0}^{M-1} x^2[n] = \frac{1}{M} \sum_{k=0}^{M-1} \left| X[k] \right|^2 . \tag{71}$$

These definitions apply to double-sided interferograms and double-sided spectra. They include the fact that the data must be realigned before it is processed. So a double-sided interferogram ends starting with zero-path difference (ZPD) up to one end, followed by the points at the other end of the sweep and finishing with the points close to ZPD. This is coherent with the fact that the fast-Fourier transform (FFT) algorithm works with the hypothesis that both the signal and the spectrum are periodic. More specifically, the pattern observed from 0 to M-1 is repeated from M to 2M-1, and so on or conversely the pattern from –M/2+1 to M/2 is repeated from M/2+1 to 3M/2, and so on. Therefore the negative frequency side, being mapped from –M/2+1 to –1, is also mapped from M/2+1 toM-1.

Suppose that the spectrum X[k] is non zero only for one spectral bin, k_0, such that:

$$X[k] = \delta[k + k_0] + \delta[k - k_0], \tag{72}$$

The use of the DFT implies that this sequence is periodic with a period M. In fact the DFT maps a periodic "time" sequence into a periodic spectral sequence. This real and even spectrum corresponds to a real and even time signal, which is:

$$x[n] = \frac{2}{M} \cos\left(2\pi \frac{k_0}{M} n \right). \tag{73}$$

Now, if the spectrum is flat over a given spectral band and zero outside this band, the discrete spectrum is a collection of N adjacent non-zero spectral bins having the same value:

$$X[k] = \sum_{k_1=k_0}^{k_0+N-1} \left(\delta[k+k_1] + \delta[k-k_1]\right), \tag{74}$$

where all non-zero spectral bins are assigned a unitary value. The corresponding time signal is therefore:

$$x[n] = \sum_{k_1=k_0}^{k_0+N-1} \frac{2}{M} \cos\left(2\pi \frac{k_1}{M} n\right). \tag{75}$$

This interferogram has its maximal value at n=0. It is given by:

$$x[0] = \sum_{k_1=k_0}^{k_0+N-1} \frac{2}{M} \cos(0) = \frac{2}{M}(k_0 + N - 1 - k_0 + 1) = \frac{2N}{M} \tag{76}$$

This shows that for N out of M/2 unitary spectral bins, the maximal interferogram value is 2N/M. Conversely if the maximal value of the time signal is one, the N non-zero spectral bins will have a M/2N value. Here we use the fact that the time signal has no DC component. If it has been present, it theoretically should be a level of 1 in the interferogram domain, corresponding to a level M for the spectral bin at 0. This is depicted in Figure 30 for a band-limited spectrum and its interferogram. It must be noticed that both the interferogram and its spectrum are folded in order to be easier to interpret.

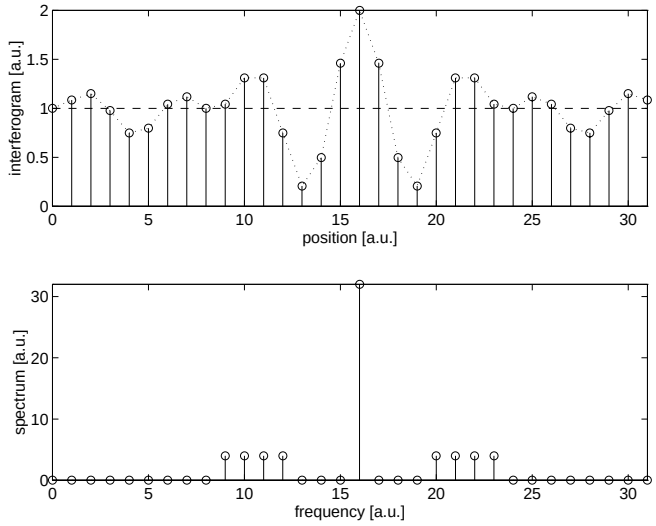

Figure 30 Interferogram and associated band-limited spectrum.

If x[n] =e[n] where e[n] is a zero-mean white noise with variance σ_e^2, the transformed signal will also be zero-mean white noise. The point is to evaluate the noise variance in this domain. Using Parseval's relation one has:

$$E\left\{\sum_{n=0}^{M-1} e^2[n]\right\} = E\left\{\frac{1}{M}\sum_{k=0}^{M-1}\left|E[k]\right|^2\right\}. \tag{77}$$

By interchanging the order of operators and expressing $|E[k]|^2$ with its real and imaginary components, one obtains:

$$\sum_{n=0}^{M-1} E\left\{e^2[n]\right\} = \frac{1}{M}\sum_{k=0}^{M-1}\left(E\left\{E_r^2[k]\right\} + E\left\{E_i^2[k]\right\}\right), \tag{78}$$

since the real and imaginary values of the DFT are uncorrelated. All the expectations in this equation are variances. The transformed noise will be equally split between the real an imaginary parts so that:

$$\sum_{n=0}^{M-1}\sigma_e^2 = \frac{1}{M}\sum_{k=0}^{M-1}(\sigma_{E_r}^2 + \sigma_{E_i}^2) = \frac{2}{M}\sum_{k=0}^{M-1}\sigma_{E_r}^2 \ . \tag{79}$$

Thus the variance of the real part of the DFT becomes:

$$\sigma_{E_r} = \sqrt{\frac{M}{2}}\sigma_e . \tag{80}$$

Combining all the results, one can then say that if an interferogram has a unitary maximal value, its SNR will be (at n=0):

$$SNR_{IGM} = 1\big/\sigma_e \ . \tag{81}$$

It is now also possible to calculate the spectral SNR for the non-zero spectral bins:

$$SNR_{SPC} = \frac{M\big/2N}{\sqrt{M\big/2}\sigma_e} = \frac{1}{N}\sqrt{\frac{M}{2}}\frac{1}{\sigma_e} = \frac{1}{N}\sqrt{\frac{M}{2}}SNR_{IGM} , \tag{82}$$

which is the desired result. We have thus related the spectral SNR to the interferogram SNR at ZPD.

7.2 SINGLE-SIDED INTERFEROGRAMS

Single-sided interferograms could be measured instead of full double-sided ones since the interferogram is theoretically even. So, in principle, a single-sided interferogram is simply mirrored prior to the evaluation of the DFT:

$$x[n] = \begin{cases} x_{SSI}[n], & 0 \le n \le \dfrac{M}{2} \\ x_{SSI}[M-n], & \dfrac{M}{2}+1 \le n \le M-1 \end{cases} . \tag{83}$$

The DFT becomes

$$X[k] = \sum_{n=0}^{\frac{M}{2}} x_{SSI}[n] e^{j2\pi \frac{k}{M} n} + \sum_{n=\frac{M}{2}+1}^{M-1} x_{SSI}[M-n] e^{j2\pi \frac{k}{M} n} \tag{84}$$

By reordering the last sum and by rearranging terms, one finally finds

$$X[k] = 2 \sum_{n=0}^{\frac{M}{2}-1} x_{SSI}[n] \cos\left(2\pi \frac{k}{M} n \right) - x_{SSI}[0] + (-1)^k x_{SSI}[M/2]. \tag{85}$$

This last result clearly shows that the DFT is real, which corresponds to an even time sequence. So a given level of interferogram, double-sided or mirrored single-sided, gives the same level in the spectrum domain.

Given Parseval's relation, the noise contribution is

$$E\left\{ \sum_{n=0}^{\frac{M}{2}} e_{SSI}^2[n] + \sum_{n=\frac{M}{2}+1}^{M-1} e_{SSI}^2[M-n] \right\} = E\left\{ \frac{1}{M} \sum_{k=0}^{M-1} \left| E[k] \right|^2 \right\}. \tag{86}$$

By interchanging the order of operators and expressing $|E[k]|^2$ only with its real component, since the time sequence is still even, one obtains:

$$\sum_{n=0}^{\frac{M}{2}} E\left\{ e_{SSI}^2[n] \right\} + \sum_{n=\frac{M}{2}+1}^{M-1} E\left\{ e_{SSI}^2[M-n] \right\} = \frac{1}{M} \sum_{k=0}^{M-1} E\left\{ E_r^2[k] \right\}. \tag{87}$$

All the expectations in this equation are variances since the stochastic processes are zero-mean,

$$\sum_{n=0}^{M-1} \sigma_e^2 = \frac{1}{M} \sum_{k=0}^{M-1} \sigma_{E_r}^2 . \tag{88}$$

Thus the variance of the real part of the DFT becomes:

$$\sigma_{E_r} = \sqrt{M} \sigma_e . \tag{89}$$

Combining all the results, one can then say that if an interferogram has a unitary maximal value, its SNR will be (at n=0):

$$SNR_{IGM} = 1 / \sigma_e . \tag{90}$$

It is now also possible to calculate the spectral SNR for the non-zero spectral bins:

$$SNR_{SPC} = \frac{M/2N}{\sqrt{M}\sigma_e} = \frac{1}{2N}\sqrt{M}\,\frac{1}{\sigma_e} = \frac{1}{2N}\sqrt{M}\,SNR_{IGM}\,, \qquad (91)$$

which is the desired result. We have thus related the spectral SNR to the interferogram SNR at ZPD. The last result shows a factor $\sqrt{2}$ with the relation obtained for the double-sided case (Equation 82), because the mirroring operation made all the noise even and put all its contribution in the real part of the spectrum.

— End of document —